Marquette University
e-Publications@Marquette

Master's Theses (2009 -) Dissertations, Theses, and Professional Projects

Development of a Quasi-Monte Carlo Method for Thermal Radiation

Joseph Farmer
Marquette University

Recommended Citation
Farmer, Joseph, "Development of a Quasi-Monte Carlo Method for Thermal Radiation" (2019). *Master's Theses (2009 -)*. 524.
https://epublications.marquette.edu/theses_open/524

DEVELOPMENT OF A QUASI-MONTE CARLO METHOD FOR THERMAL RADIATION

by

Joseph A. Farmer

A Thesis submitted to the Faculty of the Graduate School,
Marquette University,
in Partial Fulfillment of the Requirements for
the Degree of Master of Science

Milwaukee, Wisconsin

May 2019

ABSTRACT
DEVELOPMENT OF A QUASI-MONTE CARLO
METHOD FOR THERMAL RADIATION

Joseph A. Farmer

Marquette University, 2019

Radiative heat transfer in participating media is among the most challenging computational engineering problems due to the complex nonlinear, nonlocal nature of radiation transport. Many approximate methods have been developed in order to resolve radiative heat transfer in participating media; but approximate methods, by the nature of their approximations, suffer from various shortcomings both in terms of accuracy and robustness. The only methods that can resolve radiative transfer accurately in all configurations are the statistical Monte Carlo-based methods. While the Monte Carlo (MC) method is the most accurate method for resolving radiative heat transfer, it is also notoriously computationally prohibitive in large-scale simulations. To overcome this computational burden, this study details the development of a quasi-Monte Carlo (QMC) method for thermal radiation in participating media with a focus on combustion-related problems. The QMC method employs a low-discrepancy sequence (LDS) in place of the traditional random number sampling mechanism used in Monte Carlo methods to increase computational efficiency. In order to analyze the performance of the QMC method, a systematic comparison of accuracy and computational expense was performed. The QMC method was validated against formal solutions of radiative heat transfer in several one-dimensional configurations and extended to three practical combustion configurations: a turbulent jet flame, a high-pressure industrial gas turbine, and a high-pressure spray combustion chamber. The results from QMC and traditional Monte Carlo are compared against benchmark solutions for each case. It is shown that accuracy of the predicted radiation field from QMC is comparable to MC at lower computational costs. Three different low-discrepancy sequences – Sobol, Halton, and Niederreiter – were examined as part of this work. Finally, recommendations are made in terms of choice of the sequence and the number of the dimensions of the LDS for combustion-relevant configurations. In conclusion, significant improvements in computational costs and accuracy seen in the QMC method makes it a viable alternative to traditional Monte Carlo methods in high-fidelity simulations.

ACKNOWLEDGMENTS

Joseph A. Farmer

Thank you to my advisor, Dr. Somesh Roy, for the opportunity and guidance through a difficult and rewarding project! Also, special thanks to my family, friends, and Marquette community for making my experience over the past few years so enjoyable. This work was supported by the National Science Foundation (award #1756005).

DEDICATION

To my mom and dad, you were right!

TABLE OF CONTENTS

ACKNOWLEDGMENTS i

DEDICATION ii

LIST OF TABLES vi

LIST OF FIGURES vii

1 INTRODUCTION 1

1.1 Background 1

1.2 Motivation 3

1.3 Organization 3

2 SOLVING RADIATION IN PARTICIPATING MEDIA 5

2.1 Radiative Transfer Equation 5

2.2 Radiation Solvers 6

2.2.1 Optically Thin Approximation 7

2.2.2 Zonal Method 7

2.2.3 Discrete Ordinate Method 8

2.2.4 The Method of Spherical Harmonics 9

2.2.5 Statistical Methods 10

2.3 Spectral Models 10

2.3.1 Gray Model 11

2.3.2 Line-by-Line Model 12

2.3.3 Narrow Band Model 12

2.3.4 Full-Spectrum Model 13

2.4 Summary 13

3 MONTE CARLO-BASED RADIATION SOLVER 15

3.1 Introduction 15

3.2 Photon Monte Carlo Method 17

3.2.1 Overview 17

3.2.2 Random-Number Relations 18

3.2.3 Ray Tracing 22

3.3 Random and Pseudorandom Numbers for Monte Carlo Methods . 25

3.4 Advantages and Disadvantages 26

3.5 Summary 26

4 QUASI-MONTE CARLO METHOD 28

4.1 Introduction 28

4.2 Properties of Low-Discrepancy Sequences 29

4.2.1 Overview 29

4.2.2 Sobol's Sequence 30

4.3 Quasi-Monte Carlo Method in Literature 31

4.4 Quasi-Monte Carlo for Radiation in Participating Media 32

4.5 Summary 32

5 RESULTS AND DISCUSSION 34

5.1 Validation in One-Dimensional Plane-Parallel Media 35

5.2 Three-Dimensional Combustion Simulations 37

5.2.1 An Artificial Turbulent Jet Flame 37

5.2.2 A High-Pressure Gas Turbine 41

5.2.3 ECN Spray-A 44

5.2.4 Computational Efficiency and Figure of Merit 48

5.3 Summary 50

6 RECOMMENDATIONS FOR QMC 51

6.1 Choice of Low-Discrepancy Sequence 51

6.1.1 Validation in One-Dimensional Plane-Parallel Media . . . 53

6.1.2 High-Pressure Gas Turbine 54

6.2 Dimensionality of Low-Discrepancy Sequences 56

6.3 Effect of Reflective Walls 58

6.3.1 High-Pressure Gas Turbine 58

6.4 Summary 60

7 CONCLUSION 62

8 FUTURE WORK 64

BIBLIOGRAPHY 66

A APPENDIX 72

LIST OF TABLES

4.1 Calculating Sobol's sequence 31

5.1 One-dimensional validation cases. In case (2) the x [m] is the distance from one wall. 35

6.1 QMC scheme comparison 57

LIST OF FIGURES

2.1 Absorption coefficient of H_2O, CO_2, and CO at 600 K and 1 atm 11

3.1 Samples generated in a two-dimensional space illustrating the prediction of π 16

4.1 Samples generated in two-dimensional space from a PRNG 30

4.2 Samples generated in two-dimensional space from an LDS (Sobol) 30

5.1 Accuracy and convergence of QMC and MC in one-dimensional cases . . 36

5.2 SandiaDx4 configuration and geometry 38

5.3 Scalar field contours for SandiaDx4 configuration 39

5.4 Absorption field contours for SandiaDx4 configuration 40

5.5 Absorption along a line in SandiaDx4 configuration with 800,000 rays . . 40

5.6 GT configuration 41

5.7 Scalar field contours for GT configuration 42

5.8 Absorption along a line in GT configuration with 1,600,000 rays 42

5.9 Wall heat flux in GT configuration with 1,600,000 rays 43

5.10 Spray A configuration geometry 45

5.11 Scalar field contours for Spray-A configuration 46

5.12 Absorption along a line in Spray-A configuration with 1,600,000 rays . . 47

5.13 Wall heat flux in Spray-A configuration with 1,600,000 rays illustrated in Fig. 5.10 47

5.14 Figure of Merit (FoM) along two different lines of MC and QMC simulations for SandiaDx4, GT and Spray-A configurations 49

5.15 Figure of Merit (FoM) for both walls in the GT and Spray-A configurations in MC and QMC simulations. 50

6.1 Two-dimensional Niederreiter Sequence 52

6.2 Two-dimensional Halton Sequence 52

6.3 Two-dimensional Sobol's Sequence 52

6.4 Accuracy and convergence of Sobol, Halton, Niedereitter and MC in one-dimensional cases 53

6.5 GT medium radiative absorption statistics with 1,600,000 rays 55

6.6 Wall heat flux in GT configuration with 1,600,000 rays 55

6.7 GT FoMs with 1,600,000 rays 56

6.8 GT medium radiative absorption statistics with 1,600,000 rays 59

6.9 GT FoMs with 1,600,000 rays 60

6.10 GT FoMs with 1,600,000 rays 61

A.1 Flow Chart of photon Monte Carlo method 72

CHAPTER 1

INTRODUCTION

1.1 Background

Heat transfer caused by electromagnetic waves is commonly referred to as *thermal radiation* or *radiative heat transfer*. Thermal radiation can be distinguished from conduction and convection (the other two forms of heat transfer) in a number of ways. For example, radiative heat transfer does not require a medium nor an interaction between adjacent environments, whereas conduction and convection do. Conductive and convective heat transfer depend linearly on the temperature gradient, but radiative heat transfer is biquadrately dependent on temperature. These characteristics make radiation a distinct and significant mechanism for energy transfer to consider in engineering applications and environmental decisions. More intimately, thermal radiation manifests itself in a variety of ways to people *e.g.*, the sun is continuously radiating thermal energy to warm the earth, the heat from a fire is felt on the side facing the fire, the color of the sky is a function of the radiative properties of our atmosphere, and that, we feel more comfortable in a room (set to the same temperature) on a warm summer night than during a nippy winter.

The extent and effect of combustion-related pollution as it relates to climate change is arguably the most dire problem facing humanity. It is exciting to see the growing research and interest in powering today's world with renewable energy, however, combustion continues to be the primary source of energy for society and probably will be for the foreseeable future. For example, almost all propulsion systems are provided thrust through the combustion of fuel, and for many of these (*e.g.*, aircrafts, cargo ships, trucks), there are no practical zero-carbon alternatives. Combustion is amazingly powerful, but unfortunately its inefficiencies are one of the

primary causes of air pollution. This has motivated the development of high-efficiency, low-emission combustors, and, in turn, the research of high-fidelity combustion models in order to better understand combustion physics.

Combustion physics involves a wide breadth of physics and engineering disciplines, including fluid mechanics, chemical kinetics, and heat transfer, which are coupled in both space and time. Because of its complex and multidisciplinary nature, understanding and modeling combustion is an ongoing research endeavor. Comprehensive and accurate combustion models require each sub-model of the combustion system (*e.g.*, fluid mechanics, chemical kinetics, and heat transfer) to be modeled with appropriate fidelity. There has been significant improvement over the years in flow models and chemical kinetics but thermal radiation has been traditionally neglected or over-simplified. There is significant opportunity for research of accurate models for heat transfer via radiation in combustion due to the high temperature dependence of thermal radiation.

Formal solutions to the governing equation for radiative heat transfer are unavailable in relevant engineering or combustion applications *e.g.*, gas turbine combustors, internal combustion engines, industrial burners, etc., which has led to the development of a plethora of approximate methods. Although, many of the common models are unreliable in relevant combustion applications, they are widely used in commercial computational fluid dynamics (CFD) solvers to reduce computational complexity. The most robust and accurate class of radiation solvers are Monte Carlo ray tracing-based (MCRT) solvers. Monte Carlo methods are notorious for their computational expense, but with the advent of quickly increasing computational power, parallel computing and computationally efficient models, this bottleneck is rapidly fading.

The specific objective of this work is to increase the computational efficiency of a Photon Monte Carlo (PMC) method for thermal radiation. In this study, the

PMC method is modified to a quasi-Monte Carlo (QMC) for radiation in aim of reducing computational costs.

1.2 Motivation

Computational fluid dynamics (CFD) solvers are indespensible tools for research, design, and development in many applications, such as in heat transfer and combustion. In high temperature applications, thermal radiation can be the dominant form of heat transfer and can heavily influence the prediction of many quantities of interest *e.g.*, pollutant formation, flame temperature, flame struture etc. [1, 2]. There is a growing body of research showing the importance of accurate radiation modeling in combustion systems [3, 4, 5, 6, 7, 8, 9]. However, radiation modeling has traditionally been over-simplified so as to minimize the computational complexity and costs in CFD simulations. Success with the QMC method will help facilitate and push forward the ongoing research in the radiation community by providing a computationally efficient and accurate method for solving radiative heat transfer.

1.3 Organization

In order to present a systematic methodology for the development of a quasi-Monte Carlo method for thermal radiation, the thesis is divided into several sections that lay the foundations of the present knowledge in radiation theory. The literature review is encompassed within Chapters 2 - 4. Chapter 2 introduces the radiative transfer equation (RTE), approximations to the RTE, and spectral models. Chapter 3 introduces Monte Carlo methods, the difference between random and pseudorandom numbers, and the apparent advantages and disadvantages of Monte Carlo based solvers for thermal radiation. Chapter 4 introduces the concept

of a quasi-Monte Carlo algorithm and how it is distinguished from traditional Monte Carlo algorithms. Chapter 5 presents validation of QMC and a comparison of QMC and PMC. This chapter is taken almost directly from the author's under-review article [10]. Chapter 6 examines the effect of reflection in QMC and compares the choice of a low-discrepancy sequence for the QMC method. Finally, the conclusion and future work are presented in Chapters 7 and 8, respectively.

CHAPTER 2

SOLVING RADIATION IN PARTICIPATING MEDIA

2.1 Radiative Transfer Equation

In Chapter 1 the concept of thermal radiation was introduced and the influence of thermal radiation was emphasized in several ways. In this section, the governing equation for radiative heat transfer in participating media, the *radiative transfer equation* (RTE), will briefly be developed as done in [1]. The concepts developed here are integral into understanding the Monte Carlo method for thermal radiation. First, it is important to define and differentiate *participating* and *non-participating* media. Radiative transfer between two surfaces separated by a vacuum or a medium that does not interact with the transfer of electromagnetic waves (or photons) refers to non-participating media. Most practical engineering problems do not operate under such conditions, but rather, the medium participates in the radiation by absorbing, emitting, and scattering photons.

During heat transfer via radiation, photons are emitted from participating species or surfaces with a finite amount of energy into a specific direction. Along its path, radiative intensity is attenuated (loses energy) through absorption and scattering of photons to a direction outside its path (out-scattering) and augmented (gains energy) through emission and scattering into the direction of its path (in-scattering). The total attenuation of intensity is known as extinction and the extinction coefficient is defined as $\beta_\eta = \kappa_\eta + \sigma_{s\eta}$ where κ_η is the absorption coefficient, $\sigma_{s\eta}$ is the scattering coefficient, and the subscript η is the spectral variable – wavenumber, indicating that each are valid for only one wavenumber. Similarly, the total augmentation is the combination of emission and in-scattering. The emission of intensity from a given volume is proportional to the energy content

within the volume while the contribution from in-scattering comes from all directions.

Finally, the RTE, which is influenced by emission, absorption, and scattering, can be defined as

$$\frac{dI_\eta}{ds} = \hat{s} \cdot \nabla I_\eta = \kappa_\eta I_{b\eta} - \beta_\eta I_\eta + \frac{\sigma_{s\eta}}{4\pi} \int_{4\pi} I_\eta(\hat{s}) \Phi_\eta(\hat{s}_i, \hat{s}) d\Omega_i, \tag{2.1}$$

where I_η is the radiative intensity, $I_{b\eta}$ is the blackbody radiative intensity, $\Phi_\eta(\hat{s}_i, \hat{s})$ is the scattering phase function between ray directions $\hat{s}_i$ and $\hat{s}$, and Ω_i represents solid angle. The first and third term on the right-hand side of the RTE represent augmentation due to emission and in-scattering, respectively. The second term represents the total attenuation due to absorption and out-scattering of photons.

The RTE is a five-dimensional integro-differential equation for radiative intensity (three spatial and two directional dimensions). The formal solution to the RTE is only available in simple configurations like a one-dimensional slab. As such, the difficulty to solve the RTE has led to many numerical approximations to utilize in CFD simulations. The approximations are generally validated in simple one-dimensional configurations. Chapter 5 presents validation results from the quasi-Monte Carlo method for thermal radiation in a one-dimensional plane-parallel nonscattering medium enclosed by black bounding surfaces where the formal solution to the RTE is known. The following section introduces common solution techniques to account for radiative heat transfer.

2.2 Radiation Solvers

Even in one-dimensional participating media the solution to the RTE is a burdensome and challenging task because the exact solution is represented implicitly in the form of an integral equation. Furthermore, most engineering applications are multi-dimensional and nonhomogeneous with nonlinear spectral properties (κ, σ, β

and Φ) that vary highly with wavenumber and thermodynamic state of the medium. This has led to the development of many different approximations to the RTE which can be divided into two categories: deterministic methods and stochastic methods. The majority of deterministic methods used in practice are: the optically thin approximation, the zonal method, the discrete ordinate method, and the method of spherical harmonics. The statistical methods are known as Monte Carlo methods. The choice of approximation is dependent on a variety of factors such as, but not limited to, the accuracy required, the flame characteristics, the geometry of the configuration, or the solution methodology of other phenomena in the simulation.

2.2.1 Optically Thin Approximation

The optically thin (OT) approximation simplifies the RTE to only the first term on the right-hand side of Eqn. 2.1. Therefore, the OT approximation only accounts for the emission of photons and neglects the other phenomena (absorption and scattering) encountered in participating media. This method is advantageous for its computational efficiency, inherent simplicity, and is appropriate to apply when the geometry of the medium is small enough that interactions with the medium are negligible. This method can be highly disadvantageous for large geometries or with media that have high absorption coefficients (optically thick). For these reasons the OT approximation will underestimate flame temperature due to over-prediction of radiative heat loss.

2.2.2 Zonal Method

The zonal method is a common method for calculating radiative heat transfer, first introduced by Hottel and Cohen [11], that requires division of the domain volume into a finite number of subvolumes with isothermal and constant

radiative properties. An energy balance between zones (exchange areas) yields a set of nonlinear algebraic equations where radiatvie intensity can be evaluated. This method is able to produce accurate results, however it is limited to simple geomtries because the computational costs of this method are high and make coupling with the fluid mechanics calculations challenging due to the fine computational zones in the flow fields [12, 13].

2.2.3 Discrete Ordinate Method

The discrete ordinate method (DOM), or S_N approximation, was first proposed by S. Chandrasekhar [14] to resolve atmospheric radiative heat transfer. It is among the easiest to implement and computationally economical for use in commercial software. The DOM transforms the RTE into a series of partial differential equations that separate directional and spatial dependence. The distribution of radiative intensity over all solid angles is reduced to a finite number of solid angles. That is to say, the entire solid angle of 4π is discretized into n different ordinate directions symmetrically spanning the total solid angle range yielding a set of n PDEs. The integral over 4π is then approximated through numerical quadrature. Thus, the scattering integral within the RTE (which makes the formal solution difficult) is reduced to a sum of the product of radiative intensity and the scattering phase function and the corresponding weight factor due to the numerical quadrature. The order of the S_N approximation refers to the order of the quadrature scheme implemented. It can be carried out to any arbitrary order and accuracy; although, typically even-ordered schemes are used to preserve symmetry and higher-ordered schemes are computationally prohibitive.

This method suffers from two well known drawbacks known as false scattering and rays effects. False scattering, which is analogous to numerical

viscosity in CFD, is a result of the spatial discretization of the domain. The radiative intensity is smeared as the ray travels from its emission point even without radiative scattering. The remedy for this is a finer computational mesh. On the other hand, so-called ray effects is a result of the angular discretization when n directional ordinates is not enough to accurately represent radiative intensity. Rays far away from the emission zone will become far apart and some computational cells may not receive any radiative energy. The remedy for this is a coarser mesh or an increase in the order of the method. Using this method becomes a balancing act between choosing the appropriate mesh size and the number of ordinate directions.

2.2.4 The Method of Spherical Harmonics

Similar to the discrete ordinate method, the method of spherical harmonics, or P_N approximation, obtains a solution of arbitrary order or accuracy for radiative intensity by transforming the RTE into a set of PDEs. This method was introduced to resolve radiation emitted from stars by J.H. Jeans [15] and extended further by Modest and coworkers for use in combustion-related applications [16, 17, 18, 19, 20].

An exact representation for radiative intensity can be constructed by decoupling spatial and directional variations of radiative intensity through an infinite series of orthogonal spherical harmonics (function of direction only) and intensity coefficients (function of space only). However, in practice the P_N approximation truncates the sequence to order N. It has been shown that odd orders are more accurate than the next highest even order [1, 21]. The lowest order P_N approximation, P_1, is the most common implementation used due to complicated mathematics for higher order spherical harmonics, slow accuracy improvements, and the associated computational costs.

2.2.5 Statistical Methods

The statistical methods are generally referred to as Monte Carlo methods which solve the RTE in a stochastic manner. Monte Carlo ray tracing-based (MCRT) radiation solvers are the most robust and accurate class of radiation solvers. These methods provide accurate treatment of the complexities of radiation transport (*e.g.*, nongray participating media or irregular geometries) by directly mimicking the physical processes of thermal radiation. This is accomplished by emitting and tracing representative energy bundles (photons) throughout the computational domain through random-number relations. Although notorious for their computational costs, with the advent of rapidly increasing computer power and parallel computing, this bottleneck is quickly fading. Moreover, due to their corresponding accuracy, as computational efficiency improves, these methods are expected to be adopted more frequently in engineering applications. A brief discussion of Monte Carlo-based solvers is presented in Chapter 3 followed by an introduction to the quasi-Monte Carlo method for thermal radiation in Chapter 4.

2.3 Spectral Models

Up to this point, the specific influence of the wavenumber (η) has been overlooked. In nongray participating media, the RTE is only valid for a given wavenumber. Radiative properties of molecular gases are highly nonregular, nonlinear functions that fluctuate rapidly across the spectrum, adding additional complexity to radiation modeling. High resolution spectroscopy and detailed theoretical calculations have made it possible to accurately gather the strength (*i.e.*, its intensity or absorption coefficient) and position of spectral lines. The spectroscopic data is stored in large databases. In this work, data from the HITEMP2010 spectroscopic database [22] is used.

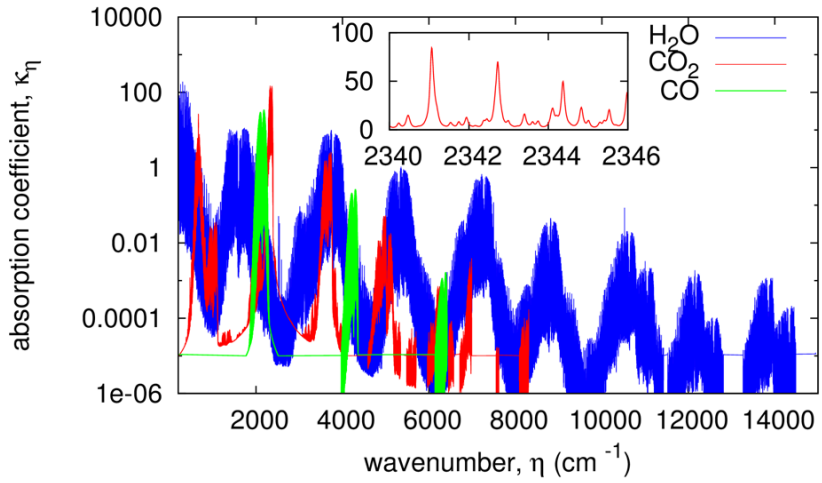

Figure 2.1: Absorption coefficient of H_2O, CO_2, and CO at 600 K and 1 atm

Figure 2.1 shows the variation of absorption coefficient for three important combustion gases – H_2O, CO_2, and CO – at 600 K and 1 atmosphere pressure. The strong variations in absorption coefficient has prompted the development of many spectral models for approximation of absorption coefficient or intensity. The accuracy of an approximate solver for radiation in participating media can be no more accurate than the accuracy of the spectral model used.

2.3.1 Gray Model

The most basic model is to simply ignore influence of wavenumber across the spectrum and assume a gray medium *i.e.*, constant radiative properties. One approximation is the Planck-mean absorption coefficient. The Planck mean is a weighted average of κ_η where the weighting function is the Planck function. It is a total absorption coefficient for the evaluation of total radiative intensity.

2.3.2 Line-by-Line Model

Line-by-line (LBL) models are the most accurate spectral models and are typically used as the benchmark solutions for other approximations. The radiative properties of inidivdual species are calculated via quantum mechanics for each wavenumber. Historically, these methods have been computationally prohibitive due to the high resolution of gas property data required and the amount of lines throughout the spectrum, which together, consume a lot of computing resources. An LBL database can contain millions of lines and could require roughly a million solutions to the RTE [2]. However, rapid increase in computational power and more efficient models have made LBL calculations more feasible. In particular, a spectral LBL database was developed for a Monte Carlo method for thermal radiation through a random-number relation by Modest and coworkers [23].

2.3.3 Narrow Band Model

In narrow band analysis a small wavenumber interval $\Delta\eta$ is used where the absorption coefficient or intensity is averaged over the interval. The assumption is made that blackbody radiative intensity $I_{b\eta}$, scattering coefficient $\sigma_{s\eta}$, and scattering phase function Φ_η are constant over $\Delta\eta$ [24]. It can be inferred from this that the rapid fluctuations of absorption coefficient are recognized to be much more than those of blackbody radiative intensity and the other radiative quantities. In principle, with a small enough $\Delta\eta$, narrow band models can be as accurate as line-by-line spectral models. Although, typically the RTE will be solved for only a few hundred $\Delta\eta$'s to save computational costs. There are a number of narrow band models but the two most popular methods are the Elsasser Model, which assumes uniform absorption coefficient over equally spaced lines, and the statistical models

where the absorption coefficient and/or line spacing are randomly determined through a probability density funciton [1].

2.3.4 Full-Spectrum Model

It can be seen with close inspection of Fig. 2.1 that over a given range of wavenumbers, the value of absorption coefficient is repeated many times. Each solution of the RTE with the same absorption coefficient yields repeated values for radiative intensity. Repeatedly conducting such calculations leads to the high computational costs for these spectral models. This has led to the development of so-called k-distributions where the absorption coefficients are reordered into a smooth, monotonically increasing, probability density function.

Narrow band k-distributions are easily extended to full-spectrum k-distributions (FSK). These essentially have the same accuracy as LBL calculations with significantly fewer evalutions of the RTE (approximately 10^5 fewer) [2]. Over the last two decades a lot of development has been made into this area which yielded a tabulated lookup table for precalculated k-distributions of gas mixtures which significantly reduced costs without sacrificing accuracy. A history of FSK for use in radiative transfer calculations can be found in [25, 26, 27, 28].

2.4 Summary

This chapter was dedicated to the development of the radiative transfer equation (RTE), the associated complexity of the radiative heat transfer problem, and the many approximations for both energy transfer and the determination of spectral properties. Accurate radiative heat transfer calculations require high-fidelity models for the radiative properties of the medium and the method employed to approximate the RTE. Various RTE approximate models were discussed but the two most common models utilized in CFD-based combustion

simulations are the method of spherical harmonics and the discrete ordinate method. However, the most robust and accurate models are the statistical methods (Monte Carlo methods), though, these are notorious for high computational costs. Of course, there is not one best-fit model for all applications – the choice depends on a variety of factors *e.g.*, accuracy required, computational availability, geometric complexity, etc. Similarly, there are a number of spectral models to determine radiative properties of the medium that have varying degrees of accuracy. Other phenomena have not been addressed in this chapter such as radiative properties of particulate media, the coupling between radiation, conduction, and convection, or, the growing research field of turbulent-radiation interactions (TRIs). These are left to the interested reader where two good starting points are [1, 2].

CHAPTER 3

MONTE CARLO-BASED RADIATION SOLVER

3.1 Introduction

Mathematics is commonly recognized as being pure or applied. In many cases, however, mathematics is independent of these denominations such that another dichotomy represents mathematics as either theoretical or experimental. An analogy can be drawn to the common theoretical and experimental physicists who draw conclusions through abstraction of systems via postulates, or observations of physical phenomena via experiments, respectively. Monte Carlo algorithms fall within the branch of experimental mathematics by way of repeated, random experimentation *i.e.*, independent of the objective of the problem. They are a broad class of statistical algorithms that numerically solve physical and mathematical problems via repeated random sampling [29].

To illustrate implementation of a Monte Carlo method, it is common to predict the mathematical constant π. To estimate π, random samples are uniformly distributed in two dimensional space in the first quadrant on the interval 0 to 1. The ratio of the area of a circle to the area of a square is represented by $\pi/4$ and is equivalent to the ratio of the number of points sampled within the unit circle (N_{in}) to the total number of points sampled (N_{tot}). Therefore, the estimate of π is equal to $4N_{in}/N_{tot}$. In this case, it is averaged over ten statistical analyses (ten independent, repeated simulations). Figure 3.1 shows the progression of accuracy for the estimated value of π with the Monte Carlo method. This illustrates the computational complexity that accompanies Monte Carlo methods, and is clearly not the most elegant determination of the mathematical constant.

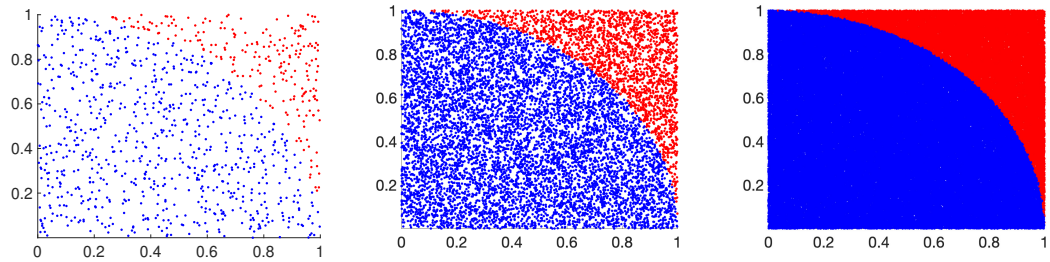

(a) ≈ 3.1188, 10^3 samples (b) ≈ 3.1387, 10^4 samples (c) ≈ 3.1416, 10^5samples

Figure 3.1: Samples generated in a two-dimensional space illustrating the prediction of π

The main advantage of Monte Carlo methods is their ability to handle complicated problems that are beyond the capabilities of theoretical mathematics. It is often convenient to use a Monte Carlo approach in conjuction with the underlying theoretical structure of the problem. For example, formal solutions to some physical phenomena (*e.g.*, the RTE) are ill-equipped to be solved by theory alone; however, the formulation of the symbolic expression or equation provides valuable insight into the physical processes undergone. With this insight, an appropriate numerical model can be constructed within the framework of a Monte Carlo approach that accounts for the physical processes of the problem.

These methods have been used in a wide vareity of fields, including science, engineering, mathematics, finance and many more. In addition, Monte Carlo schemes have been developed for radiative transport outside of the realm of combustion. For example, applications include biomedical imaging, photodynamic therapy, or radiation therapy, where the numerical model predicts patient radiation dosage for cancerous cells [30, 31]. Similarly, Monte Carlo ray tracing is the most accurate form of 3D rendering for computer graphics [32]. Some other interesting application areas are: predictive weather models, such as ensemble forecasting, where Monte Carlo methods are used to reduce uncertainty in predicted weather patterns [33], using simulated annealing with a Monte Carlo method for the

modeling of solar cells [34], and estimation of the partition function in common ferromagentic models such as the Potts model [35].

Monte Carlo methods are dependent on the sampling of random numbers, usually done via a psuedorandom number generator (PRNG). In simple configurations, such as the estimation of π or one-dimensional radiative heat transfer, roughly 10^5 samples are needed for an accurate solution. For more complex problems such as combustion, the method could require upwards of 10^8 samples; although, these are merely guidelines. To analyze the performance of a Monte Carlo method, the statistical error (*i.e.*, standard deviation) of a quantity of interest is used to measure accuracy and convergence. The statistical limit of the standard deviation is represented by $O\left(N^{-1/2}\right)$ where N is the number of samples.

3.2 Photon Monte Carlo Method

3.2.1 Overview

Monte Carlo methods are one of several computational methods to approximate radiative heat transfer. Among them, the *photon Monte Carlo* (PMC) method is the most accurate and can be applied to problems of arbitrary complexity. In combustion, photons (energy) are continuously emitted from hot gas molecules and surfaces into random direction with distinct wavenumbers [36]. The PMC method solves the spectral RTE (Equation 2.1) by statistically mimicking the physics of radiation *i.e.*, emitting, absorbing, and scattering of photons throughout the computational domain. This is accomplished by randomly emitting and tracking a statistically significant number of representative photons (or rays). Emission of a ray in the PMC method requires the development of six random-number relations. Specifically, six random numbers are required to emit each individual ray - three for the emission origin $(\mathcal{R}_x, \mathcal{R}_y, \mathcal{R}_z)$, two for the

propagation direction ($\mathcal{R}_\theta, \mathcal{R}_\psi$), and one for wavenumber ($\mathcal{R}_\eta$) [1, 36, 37]. For a comparison between common radiation solvers and an implementation of the PMC method used in this work please see [7, 6].

3.2.2 Random-Number Relations

Random-number relations are used in the PMC method to pick statistically meaningful energy bundles according to probability distributions. The location, directions, and wavenumbers of emission, are accordingly chosen from probability distributions and will be shown from a volume V_k here.

Emission Location

The emissive energy distribution throughout a computational domain influences the emission origin of rays *i.e.*, hot zones will have high concentrations of molecular gases that continuously emit rays (strong emission) while cold zones will tend to have weak emission. In order to pick statistically significant emission points, the PMC method must emit more rays from hot zones than cold zones. This is achieved by relating the emission origin's random numbers to the emissive energy. The total emission from a volume is

$$E_k = \int_{V_k} 4\kappa_P \sigma T^4 dV \tag{3.1}$$

where κ_P is the Planck-mean absorption coefficient, σ is Stefan Boltamann's constant and T is temperature. The integral over a volume is equivalently represented in Cartesian coordinates as

$$E_k = \int_0^X \left(\int_0^Y \int_0^Z 4\kappa_P \sigma T^4 dz dy \right) dx = \int_0^X E_k'(x) dx. \tag{3.2}$$

Equation. 3.2 can also be rewritten as a probability density function

$$\mathcal{R}_x = \frac{1}{E_k} \int_0^x E_k' dx \tag{3.3}$$

where $\mathcal{R}_x$ is the probability that x-coordinate location will be located between 0 and x and is known as a cumulative distribution function. By definition, the probability that the x-coordinate location falls between 0 and ∞ is, of course, $\mathcal{R}(x \to \infty) = 1$. Inverting this relationship yields an emission point as a function of random number $\mathcal{R}_x$

$$x = x(\mathcal{R}_x) \tag{3.4}$$

A similar analysis can be done for both y and z coordinates as well which yields y-location as a function of both $\mathcal{R}_y$ and x while z-location is a function of $\mathcal{R}_z$, x, and y:

$$y = y(\mathcal{R}_y, x), \tag{3.5}$$

$$z = z(\mathcal{R}_z, x, y). \tag{3.6}$$

The choices for x, y and z become independent of each other if the medium is isothermal and has a uniform absorption coefficient.

Direction of Emission

Emission from within a medium is isotropic *i.e.*, rays are released in all directions with equal probability. The solid angle $4\pi = \int_0^{2\pi} \int_0^{\pi} sin\theta d\theta d\psi$ contains all possible directions for a ray to travel. The direction coordinates are

$$\psi = 2\pi\mathcal{R}_\psi, \tag{3.7}$$

and

$$\theta = cos^{-1}(1 - 2\mathcal{R}_\theta). \tag{3.8}$$

Similarly, most surfaces are isotropic which simplifies the surface-emission relationship. Therefore, for a diffuse emitter, azimuthal angle remains unchanged while the polar angle is now represented as

$$\theta = sin^{-1}\sqrt{\mathcal{R}_\theta} \tag{3.9}$$

Wavenumber of Emission

Generation of spectral random-number relations is a complicated endeavor. In gray gas analyses, no spectral model is required because rays are given identical absorption coefficeints. In nongray analyses, the Monte Carlo-based spectral model introduced in Chapter 2 developed by Wang, Modest, and Ren [36, 37] is used to efficiently determine wavenumber and absorption coefficient. In this model, a tabulated random-number wavenumber database developed in [23] facilitates the prediction of wavenumber and the corresponding absorption coefficient through the random number $\mathcal{R}_\eta$. The database covers relations for many important radiatively participating combustion species (H_2O, CO_2, CO, CH_4, and C_2H_4) for a temperature range of 300 K to 3000 K and pressures up to 80 bar.

Similar to the development of the random-number relation for the x-coordinate, the probability that an emitted ray will have a wavenumber between 0 and η is given by

$$\mathcal{R}_\eta = \frac{1}{E_{tot}} \int_0^\eta \kappa_\eta I_{b\eta} d\eta. \tag{3.10}$$

and inverting this yields

$$\eta = \eta \left(\mathcal{R}_\eta, x, y, z \right). \tag{3.11}$$

In most participating media calculations however, there exists a mixture with n_s species, where the total emission E_{tot} from the gas mixture is

$$E_{tot} = \sum_{i=1}^{n_s} E_i \tag{3.12}$$

with E_i being the emission from species i, which implies emission from individual species is independent from each other. Emission from species i is defined as

$$E_i = \int_0^\infty \kappa_{\eta,i} I_{b\eta} d\eta. \tag{3.13}$$

Now, Eqn. 3.10 can be written in terms of species s by

$$\mathcal{R}_\eta = \frac{\sum_{i=1}^{s-1} E_i + \int_0^\eta \kappa_{\eta,s} I_{b\eta} d\eta}{E_{tot}} \tag{3.14}$$

which shows that the fractional energy $\mathcal{R}_\eta$ is the ratio of the sum of E_i over all species with index smaller than s plus the energy of species s evaluated from 0 to η to the total emission.

The emitting species can be determined after drawing random-number $\mathcal{R}_\eta$ according to the random-number relation:

$$s = j \qquad \text{if} \qquad \frac{\sum_{i=1}^{j-1} E_i}{E_{tot}} < \mathcal{R}_\eta \leq \frac{\sum_{i=1}^{j} E_i}{E_{tot}} \tag{3.15}$$

which ensures the wavenumbers for species i are related to the fractional emission of the species. Then $\mathcal{R}_\eta$ is rescaled to

$$0 \leq \mathcal{R}_{\eta,s} = \frac{\mathcal{R}_\eta E_{tot} - \sum_{i=1}^{j-1} E_i}{E_j} < 1 \tag{3.16}$$

where $\mathcal{R}_{\eta,s}$ selects photons from species s with equal strength and the wavenumbers selected for species i are found through the equivalent probability density function in Eqn. 3.10 modified for each species by

$$\mathcal{R}_{\eta,i} = \frac{\pi}{\kappa_{P,i}\sigma T^4} \int_0^\eta \kappa_{\eta,i} I_{b\eta} d\eta. \tag{3.17}$$

Therefore, once species s is determined, the wavenumber and corresponding absorption coefficient can be found directly from the corresponding $\mathcal{R}_\eta$–η database. The database has the form of

$$\eta = f_{\eta,i}\left(\mathcal{R}_{\eta,i}, T, x_i\right), \qquad \kappa_{\eta,i} = f_{\eta,i}\left(\eta, T, x_i\right), \qquad i = 1, 2, ..., n_s \tag{3.18}$$

where x_i is the mole fraction of species i.

Inversion of Random-Number Relations

Inversion of the random-number relations is not immediately obvious for the emission points and wavenumbers because they cannot be inverted explicitly. Consider, for simplicity's sake, the determination of wavenumber for a flat black surface. Equation 3.10 simplifies to

$$\mathcal{R}_\eta = \frac{1}{\sigma T^4} \int_0^\eta E_{b\eta} d\eta = f(\eta T). \tag{3.19}$$

Note in this example there is no dependence on x and y coordinates unlike Eqn. 3.11. Here, the end-goal is $\eta T = f^{-1}(\mathcal{R}_\eta)$. An efficient way of achieving this was developed in [38] where the authors implement a cubic spline to determine values of $(\eta T)_j$ for an equally spaced sequence *i.e.*,

$$(\eta T)_j = f^{-1}\left(\mathcal{R}_\eta = \frac{j}{J}\right), \qquad j = 0, 1, ..., J. \tag{3.20}$$

Therefore, if the drawn random number is between two values of the equally spaced sequence, the ηT can be simply determined via linear interpolation.

The random-number relations developed in the prior section are depend on additional variables. Therefore, in the general case, they will require interpolations of increasing order for each additional dependent variable *e.g.*, a double interpolation for $y = y(\mathcal{R}_y, x)$ or triple interpolation for $z = z(\mathcal{R}_z, x, y)$. Within the finite volume framework of this implementation, this is not needed. Each cell has all uniform properties.

3.2.3 Ray Tracing

In the Monte Carlo method for thermal radiation, ray tracing is the fundamental process for radiative energy transfer. Conceptually, ray tracing involves tracking the history of photons through space. The path of a particular

photon forms a *ray*. Ray tracing in the Monte Carlo method is realized through a dichotomy between energy transfer and numerical scheme.

Energy Transfer

Throughout the photon's journey, energy is traditionally deposited into an absorbing medium, or at absorbing walls, in one of two different ways: (1) the standard method (2) an energy partitioning scheme. In both cases, first the initial energy content must be determined for each ray within a finite volume. The initial energy E^0 for each ray is found at each computational cell i by $E^0 = {}^{E_i}/_{N_i}$ where E_i is the local energy content and N_i is the number of rays emitted from that cell. The number of rays emitted from a given volume is the result of the random-number relations for emission location developed in the previous section. When the whole amount of energy from a given ray is attenuated, the ray is terminated and the next ray launches.

In the standard Monte Carlo method of energy dissipation, the distance a ray travels in participating media is predetermined by a random-number relation ($\mathcal{R}_\tau$) to the optical thickness τ. Optical thickness is a relation to the transmissivity of a gas layer; and optical thickness based on extinction (β_η) is

$$\tau_\eta = \int_0^s \beta_\eta ds \tag{3.21}$$

where s is the path length. Thus, the quantity τ_η measures the ability of the path length to attenuate a photon. The path length in the standard scheme is then

$$s = \frac{1}{\tau_\eta} \ln \mathcal{R}_\tau \tag{3.22}$$

In this method, the energy content (E^0) of the photon is donated completely to the subvolume it is extinguished in. This comes with a few well known disadvantages. In optically thick media, photons emitted from the interior of a medium will rarely

travel to walls before being absorbed, when in many engineering applications, wall heat fluxes are of primary interest. In optically thin media, it is just the opposite, the lack of absorption within the medium results in poor statistical analysis for open configurations and/or reflective walls.

Alternatively, to alleviate some of these issues and eliminate the need for a random-number relation, an energy partitioning scheme is employed in this implementation of the PMC method. This scheme continuously depletes the energy content of each photon. The energy is attenuated by donating an amount $\Delta E = E^0(1 - e^{-\tau_\eta})$ to the medium. Thus, the energy content of the ray is an exponential decay function represented by $E = E^0 e^{-\tau_\eta}$. This guarantees, regardless of optical thickness, that each photon will contribute to the statistics of the method which yields faster convergence.

Numerical Scheme

The numerical scheme for ray tracing is the most computationally intensive routine for the Monte Carlo method. In this implementation, approximately 90% of the computational costs are due to tracing while only 10% are due to determination of random-number relations. Ray tracing requires knowledge of the computational mesh *e.g.*, the types of cells (hexahedral, tetrahedral, etc.). Each ray undergoes a thorough face-line intersection search that can be influenced by a variety of factors, such as the energy content of the ray, the face that the ray is destined to intersect (boundary surface or cell), or whether it passes through an intersection point of two cells. The journey of a photon can be realized by the following 7 step iterative process:

1. Identify emitting cell number
2. Select emitting location, direction, and wavenumber
3. Find the intersection face by checking each possible face

4. If photon intersects a boundary surface or participating media; the ray is absorbed, reflected, or scattered
5. If the intersection point is the face of another cell, identify new cell
6. Repeat items 3–6 until photon is terminated (left enclosure or absorbed)
7. Launch next photon.

3.3 Random and Pseudorandom Numbers for Monte Carlo Methods

Random sampling has been shown to have a decisive role in the computational Monte Carlo method. Within the framework of a deterministic machine (*e.g.*, computer) the generation of "random" samples seems to be paradoxical. After all, most programs are hopefully written with the intent to be repeatable and predictable. In the same breath, it should seemingly be an easy task for any decent programmer to write a program that spits out numbers. This class of deterministic computational algorithms are coined *pseudorandom number generators* (PRNG) which are designed to satisfy certain statistical properties of a uniform random distribution [39, 40]. However fun it may be to philosophically debate this concept of *randomness*, it is left behind for a more pragmatic view. In fact, true random numbers can be generated from a device called a hardware random number generator by means of a physical process such as thermal noise, atmospheric noise, or shot noise. However, these are typically computationally prohibitive, so a PRNG is preferred for most applications. The properties of a PRNG are described in detail in literature, but in general these should uniformly generate statistically independent numbers on the interval from 0 to 1 [40]. Additionally, F. James [39] emphasizes that a PRNG should have a good distrbution *i.e.*, randomness, a long period *i.e.*, the point at which the sequence repeats, and repeatability. Of course, the authenticity of the *randomness* of a sequence can usually be distinquished *a posteriori* through reason by the eye of an independent, impartial observer (*e.g.*, see

Kant's: Critique of Pure Reason [41] or Knuth [42] for philosophical background and discussion).

3.4 Advantages and Disadvantages

Historically, Monte Carlo methods have been employed for solving radiation merely to obtain a benchmark solution for comparison with other approximate solvers. There is rightful justification for this approach. The statistical limit of Monte Carlo methods is represented by $O\left(N^{-1/2}\right)$ meaning an accuracy increase of tenfold requires a hundredfold increase in number of samples used. This, coupled with the fact that Monte Carlo methods are based upon *repeated* sampling, left Monte Carlo methods as computationally prohibitive for use in commercial CFD software. However, in the present we simply don't need to worry about historical limitations of computers. The rise in computational efficiency, parallel computing, and efficient radiative sub-models have not only made Monte Carlo methods feasible, but arguably *preferred* due to the corresponding accuracy and ease-of-use for even the most complex geometries.

3.5 Summary

The strategy of resolving the radiative heat transfer problem via a Photon Monte Carlo (PMC) method was discussed in this chapter. The PMC method accurately predicts radiative energy transfer through emission and tracing of statistically meaningful energy bundles (photons). This process directly mimics the physics of radiation (*i.e.*, emission, absorption, reflection and scattering) through the sampling of photons via random-number relations. Appropriate random-number relations were developed to emphasize the importance of drawing statistically significant emission locations, directions, and wavenumbers. After determining

emission location, direction of propogation, and wavenumber of emission, the photon is launched and traced throughout the computational domain. Ray tracing is the most computationally expensive routine in the PMC method because of the exhaustive ray intersection search that occurs at each computational cell. The energy partitioning scheme helped in alleviating some computational cost, however the main bottleneck is the number of photons needed to accurately represent radiative heat transfer. In the next chapter, a quasi-Monte Carlo method is developed as an extension to the PMC method. The methodology change only considers the physical sampling of photons. Therefore, the random-number relations, ray tracing schemes, and determination of spectral properties remain unchanged. Quasi-Monte Carlo methods have been shown in literature to require less computational effort to achieve similar levels of accuracy to traditional Monte Carlo schemes in other fields. Achieving similar results with the PMC method will significantly reduce the number of photons needed for an accurate solution thereby considerably decreasing computational effort.

CHAPTER 4

QUASI-MONTE CARLO METHOD

4.1 Introduction

Up to this point, it has been shown that uniformly distributing N random points in n-space yields a probabilistic error bound of $O\left(N^{-1/2}\right)$ for traditional Monte Carlo methods. This can be prohibitively slow for many applications. Modest improvements to this could yield substantial impact due to the prevalence of Monte Carlo methods and similarly, for applications that would benefit from employing a Monte Carlo scheme.

One alternative to uniform random points is to sample specific, equidistant points from 0 to 1 exactly one time, in any order, with arbitrary precision. This yields a deterministic Monte Carlo method with error that decreases by N^{-1} [43]. This seems to be a fair way of constructing a sequence, and eliminates the need for random sampling. The difficulty, then, is to determine *a priori* how precise the sequence needs to be constructed. Moreover, the simulation must then sample every point, and if more accuracy is needed, the simulation will have to restart and a finer grid must be constructed.

Alternatively, a more robust sequence can be created that distributes points in some fashion that is *self-avoiding* so as to minimize clustering and gaps within n-space. These sequences are referred to as low-discrepancy sequences (LDS) and are a common technique to fill a domain of interest more quickly and evenly than random sampling. Typically, the *quasi* modifier is used to distinguish LDS-based Monte Carlo methods from traditional Monte Carlo methods *i.e.*, these are referred to as quasi-Monte Carlo methods (QMC).

The QMC method yields a much better, deterministic error bound of $O\left(N^{-1}(\log N)^{s-1}\right)$ where s is the dimensionality of the sequence [44]. Therefore, with the same computational effort, the QMC method can achieve much higher accuracy than the Monte Carlo method.

4.2 Properties of Low-Discrepancy Sequences

4.2.1 Overview

Alas, we have arrived at the alternative to the pseudorandom number generator (PRNG). Thankfully, there will be no need to debate the authenticity of randomness within the framework of a deterministic machine; sorry, Philosophy! *Low-discrepancy sequences* (LDS) are deterministic algorithms written with the intent to be repeatable, predictable, and that favors a distribution of *uniformity* over *randomness*. Figure 4.1 and 4.2 shows a comparison of a PRNG and a common LDS (Sobol's sequence). Notably, Fig. 4.1 shows that random samples tend to form clusters or gaps within the sample space while Fig. 4.2 shows samples that look to be equidistant throughout the sample space and generated in a correlated manner *i.e.*, these sequences will fill a n-space with n-tuples more evenly and quickly than a PRNG [43]. The pattern that arises from an LDS is easily discernible *e.g.*, Fig. 4.2(b) and 4.2(c) show that the points lie on obvious diagonals, however this feature is not expected to influence the results. Furthermore, at any point, or for any subset of the sequence, the truncated sequence will tend to have the same properties as the larger LDS. Intuitively, discrepancy refers to the spacing of the points within the sequence. Therefore, the lower the discrepancy, the more equal the spacing.

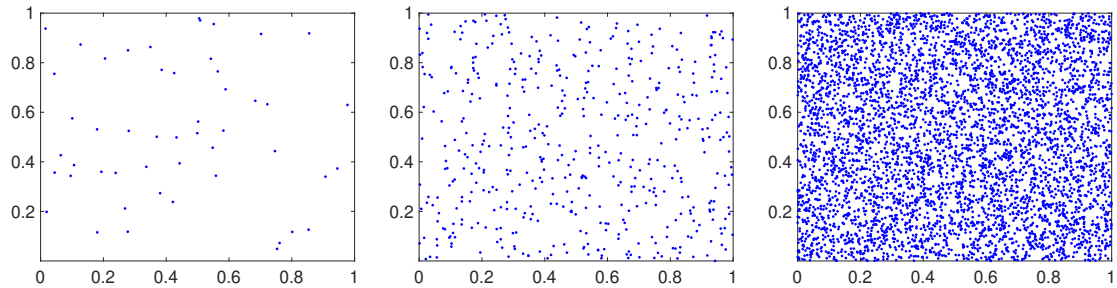

(a) 50 Samples (b) 500 Samples (c) 5000 Samples

Figure 4.1: Samples generated in two-dimensional space from a PRNG

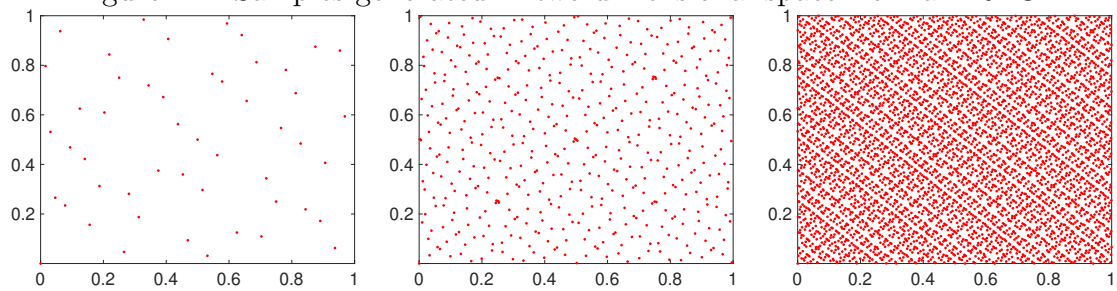

(a) 50 Samples (b) 500 Samples (c) 5000 Samples

Figure 4.2: Samples generated in two-dimensional space from an LDS (Sobol)

4.2.2 Sobol's Sequence

Sobol's sequence is an s-dimensional low-discrepancy or (t, s) sequence in base 2 which is designed to have uniform distribution behavior. In this exposition, a more utilitarian illustration of Sobol's sequence is provided. Specific details and derivations of properties (such as discrepancy) for such sequences are left to the interested, rather, daring reader (*e.g.*, see Chapter 4 of [45]). Nevertheless, this sequence has a central importance to the research in this project, therefore, it is appropriate to show a brief development of the first few points for this LDS. A full development of Sobol's original sequence can be found in [46]. However, a faster method was developed by [47] that will be the focus here and the derivation will follow the example in [48]. To generate Sobol's sequence, the first step is to create a set of direction numbers $\nu_1, \nu_2, \nu_3, ..., \nu_i$, each in binary form which are determined from the coefficients of a primitive (irreducible) polynomial. For example Eqn. 4.1 is

Table 4.1: Calculating Sobol's sequence

i	m_i	Binary i	Binary ν_i	x_i
1	1	$(0001)_2$	$(0.0100)_2$	$1/2$
2	3	$(0010)_2$	$(0.1100)_2$	$1/4$
3	7	$(0011)_2$	$(0.1110)_2$	$3/4$
4	5	$(0100)_2$	$(0.0101)_2$	$1/8$
5	7	$(0101)_2$	$(0.00111)_2$	$5/8$
6	43	$(0110)_2$	$(0.101011)_2$	$3/8$
$\vdots$				$\vdots$
100				$99/128$
101				$19/128$
102				$83/128$

a 3rd degree primitive polynomial.

$$x^3 + x + 1 \tag{4.1}$$

Then, ν_i can be calculated by $\nu_i = {}^{m_i}/_{2^i}$ where m_1, m_2, and m_3 are chosen such that $m_i < 2^i$ and the following m_i are generated by a recurrence obtained from Eqn. 4.1.

$$m_i = 4m_{i-2} \oplus 8m_{i-3} \oplus m_{i-3} \tag{4.2}$$

where the $\oplus$ is a bit-by-bit exclusive-or operator. Finally, the Sobol sequence is generated by the simple equation

$$x_{i+1} = x_i \oplus \nu_c \tag{4.3}$$

where the subscript c refers to the position of the rightmost zero in the binary representation of i and x_0 is initialized to zero. Here only a few numbers of Sobol's sequence are shown for brevity. See Table 4.1 for results.

4.3 Quasi-Monte Carlo Method in Literature

Similar to the traditional Monte Carlo method, quasi-Monte Carlo methods have been around for some time, with the first models being introduced in the

1950s. Numerical integration dominates the vast majority of the development and applications for quasi-Monte Carlo methods [44, 49]. For example, Babovsky et al. [50] showed that Halton and Hammersley sequences show improvement for the simulation of Boltzmann's equation. Ohbuchi and Aono [51] showed that the QMC method outperforms the Monte Carlo method in terms of speed and accuracy in solving the global illumination problem. In finance, prediction of of both single stock and multi-stock prices show faster convergence rates with the QMC method [52].

4.4 Quasi-Monte Carlo for Radiation in Participating Media

As discussed earlier, radiative heat transfer in the PMC method is accounted for by emitting and tracing a statistically meaningful sample of representative photons (rays) that carry a finite amount of energy. In this work a *quasi-Monte Carlo* (QMC) method for thermal radiation in participating media is proposed to improve upon the PMC method in terms of its accuracy and computational efficiency. The QMC method replaces the random numbers in the PMC method with a six-dimensional Sobol sequence. Therefore the six random numbers, emission origin $(\mathcal{R}_x, \mathcal{R}_y, \mathcal{R}_z)$, propagation direction $(\mathcal{R}_\theta, \mathcal{R}_\psi)$, and wavenumbers of emission $(\mathcal{R}_\eta)$, are substituted with $\mathcal{S}_j^1, \mathcal{S}_j^2, \ldots, \mathcal{S}_j^6$ in QMC, where $\mathcal{S}_j^n$ indicates j^{th} number in n^{th} dimension of the Sobol sequence. Where $\mathcal{S}_j^1, \mathcal{S}_j^2, \mathcal{S}_j^3$ refer to the emission origin, $\mathcal{S}_j^4, \mathcal{S}_j^5$ correspond to the propagation direction, and $\mathcal{S}_j^6$ is for the wavenumbers.

4.5 Summary

In this chapter, a breviloquent interpretation of the quasi-Monte Carlo (QMC) method for thermal radiation was developed. The QMC method is, in essence, the Photon Monte Carlo (PMC) method modified with a well-proportioned, aesthetically pleasing, surrogate sequence for the aforementioned psuedorandom

number generator. Ultimately, this exposition is concerned with the validation of the QMC method in radiative heat transfer problems while simultaneously measuring its performance against the traditional PMC implementation. Thus, this is the conclusion of the literature review for this work. Hereafter, a systematic study of the QMC method is performed. Chapter 5 divulges results for the QMC method with a six-dimensional Sobol sequence. Then, Chapter 6 analyzes special conditions of radiation and compares different low-discrepancy sequences for use in QMC.

CHAPTER 5

RESULTS AND DISCUSSION

In this section we present validation of the quasi-Monte Carlo (QMC) method for thermal radiation followed by a systematic performance comparison of the QMC and conventional Monte Carlo (MC) in multiple combustion-related configurations. The QMC scheme is validated against exact analytical solutions which are only available in simple configurations. We present results from a series of one-dimensional plane-parallel media configurations with both gray and nongray media. Then, we present three distinct, nongray combustion configurations. The first case is a turbulent jet flame with only nongray gases without any walls. The second case is a high-pressure gas turbine with nongray gases and hot walls. The final case presents a scenario of a high-pressure combustion chamber with hot walls where both gas and soot participate in radiation.

Both validation and performance evaluation are done based on either local radiative heat source (*i.e.*, divergence of local radiative heat flux, $\nabla \cdot Q$ [W/m^3]), local radiative absorption (Q_{abs} [W/m^3]), or wall heat flux (Q''_{wall} [W/m^2]) as appropriate for each test configuration. Since this implementation is based on a finite volume framework, the local root-mean-square (RMS) relative error is defined at each computational finite volume cell (index i) as

$$\epsilon_i = \left[\frac{1}{S} \sum_{s=1}^{S} \left(\frac{q_i^s}{q_i^o} - 1 \right)^2 \right]^{1/2}, \tag{5.1}$$

where q refers to the target variable (*i.e.*, $\nabla \cdot Q$ or Q_{abs} or Q''_{wall}), S refers to the number of statistical runs, q_i^s is from the Monte Carlo simulation, and q_i^o is from the analytical or benchmark solution. All configurations with the MC method use $S = 10$ statistical runs. On the other hand, QMC only requires one statistical run because of its use of a deterministic sequence *i.e.*, any two independent runs will

generate the same sequence. Additionally, as done in [53], comparison of "efficiency" of Monte Carlo schemes are done via a "figure of merit" (FoM) which also takes into account computational time. In this work, FoM is calculated based on spatially-averaged RMS relative error ($\bar{\epsilon}$)

$$\text{FoM} = \frac{1}{\bar{\epsilon}^2 t}, \tag{5.2}$$

where t is the simulation time. A high FoM score is indicative of a good Monte Carlo simulation *i.e.*, low error at low computational cost.

5.1 Validation in One-Dimensional Plane-Parallel Media

The configuration used for validation is a one-dimensional gas slab bounded by two parallel, black walls separated by 0.1 m. Several combinations of temperature and absorption coefficient profiles were tested for validation and only three representative cases are presented for brevity. These cases presented here are two with gray medium and one nongray medium as listed in Table 5.1. The gray participating media was defined by imposing a specific profile of Planck-mean absorption coefficient (κ_P). The nongray medium consisted of 20% (by mole) CO_2 and rest of the medium was radiatively non-participating. A line-by-line (LBL) database obtained from HITEMP spectroscopic database [22] was used to evaluate then nongray radiative properties of CO_2.

Table 5.1: One-dimensional validation cases. In case (2) the x [m] is the distance from one wall.

Case	(1)	(2)	(3)
Abs. Coeff.	gray, $\kappa_P = 1$ m^{-1}	gray, $\kappa_P(x) = 1 + 750x$ m^{-1}	nongray LBL
T_{medium}	1200 K	$T(x) = 1700 - 5000x$ K	2000 K
Walls	800 K, black	800 K, black	cold, black

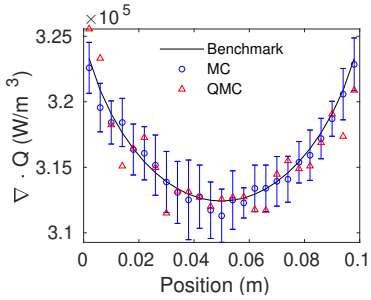

(a) Comparison of $\nabla \cdot Q$ for simulations with 20,000 rays (Case 1)

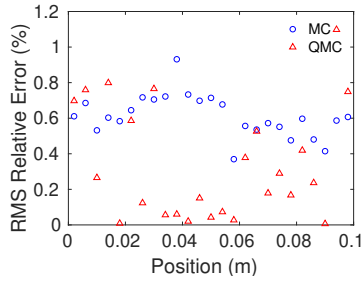

(b) RMS relative error (ϵ) for simulations with 20,000 rays (Case 1)

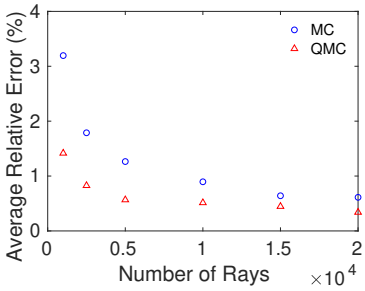

(c) Decrease in average error ($\bar{\epsilon}$) with number of rays (Case 1)

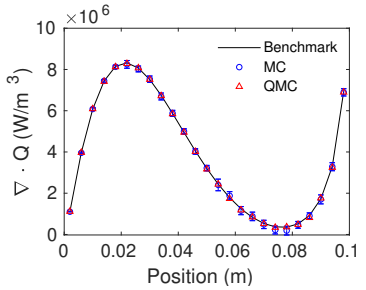

(d) Comparison of $\nabla \cdot Q$ for simulations with 75,000 rays (Case 2)

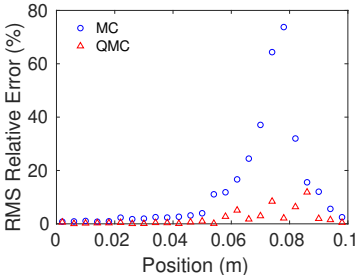

(e) RMS relative error (ϵ) for simulations with 75,000 rays (Case 2)

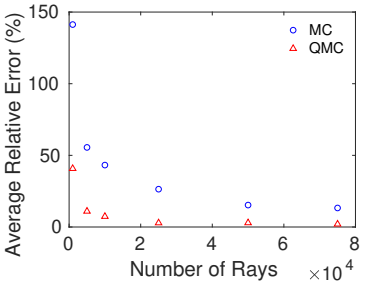

(f) Decrease in average error ($\bar{\epsilon}$) with number of rays (Case 2)

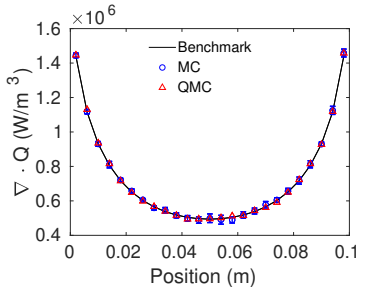

(g) Comparison of $\nabla \cdot Q$ for simulations with 100,000 rays (Case 3)

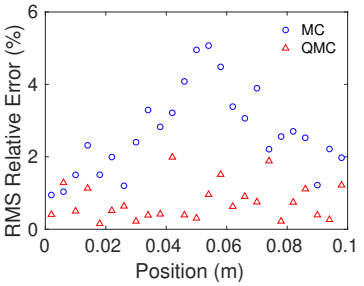

(h) RMS relative error (ϵ) for simulations with 100,000 rays (Case 3)

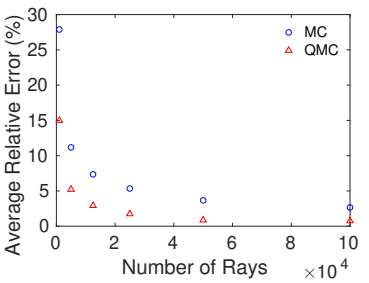

(i) Decrease in average error ($\bar{\epsilon}$) with number of rays (Case 3)

Figure 5.1: Accuracy and convergence of QMC and MC in one-dimensional cases

The results for the three cases are shown in Fig. 5.1. Figures 5.1(a), 5.1(d), and 5.1(g) shows the comparison of $\nabla \cdot Q$ calculated from the MC, QMC, along with the analytical solution. Both methods show good agreement with the analytical solution in all cases. The variation in local RMS error (ϵ_i) can be seen in Figs. 5.1(b), 5.1(e), and 5.1(h). In all three cases local error from QMC is generally lower than that from MC. Finally, Figs. 5.1(c), 5.1(f), and 5.1(i) show the "convergence rate" of QMC and MC. The convergence rate is defined as how fast the average relative RMS error ($\bar{\epsilon}$) decrease with increase in the number of rays. Both QMC and MC show a similar rate, but due to lower error (as seen in Figs. 5.1(b), 5.1(e), and 5.1(h)) QMC converges quicker than MC.

5.2 Three-Dimensional Combustion Simulations

5.2.1 An Artificial Turbulent Jet Flame

The first case considered here is an artificial flame derived from Sandia Flame D [54]. The original Sandia Flame D is an optically thin flame and may not be well-suited for radiation studies. Therefore, we artificially increased the optical thickness of the flame by quadrupling the jet diameter (increased from 7.2 mm to 28.8 mm) while decreasing the velocity (from 49.6 m/s to 12.4 m/s) to keep the Reynolds number constant. This change increases the net radiative heat transfer rate by approximately two orders of magnitude [6]. This artificial flame, here referred as SandiaDx4, was used to study effect of turbulence-radiation interaction (TRI) by several researchers [6, 55, 9]. An instaneous snapshot of this flame taken from the work of [6] is used as the first three-dimensional configuration for this study. The snapshot is an axisymmetric wedge that has 3,325 computational finite volume cells. The configuration is shown in Fig. 5.2. The scalar fields of this snapshot can be seen in Fig. 5.3. Three gas-phase species – CO_2, CO, and H_2O –

are used as the participating media. The nongray line-by-line (LBL) radiative properties of these species are obtained from the HITEMP2010 spectroscopic database [22]. For error estimation, a benchmark solution is obtained using 50 statistical runs of an MC simulation using 5×10^6 rays. In all of the three-dimensional cases, the local radiative absorption (Q_{abs} [W/m^3]) is used to measure accuracy of simulations. Because of the presence of strong optically thick regions, the radiative source term may locally become near-zero, leading to numerical issues in calculation of relative error. Additionally, local emission can be determined completely based on the thermochemical state of a computational cell and the uncertainty of the radiative transfer in MC/QMC comes from the randomness in resolving the absorption term. Hence, unless otherwise mentioned, we use the local radiative absorption as our performance metric in three-dimensional cases.

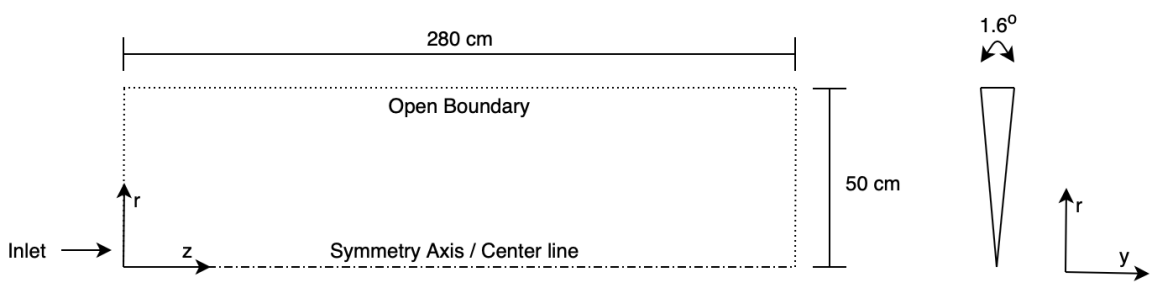

Figure 5.2: SandiaDx4 configuration and geometry

The scalar field of radiative source term from the benchmark, MC, and QMC shown in Fig. 5.4 show almost identical results from three simulations. Figure 5.5 shows two radial profiles of absorption at two different axial locations marked in Fig. 5.3 at $z = 1.0$ m and 1.43 m. Both MC and QMC were run with 800,000 rays. The MC simulation was run $S = 10$ times to obtain the statistical average and standard deviation. Error bars on the MC result represent one standard deviation.

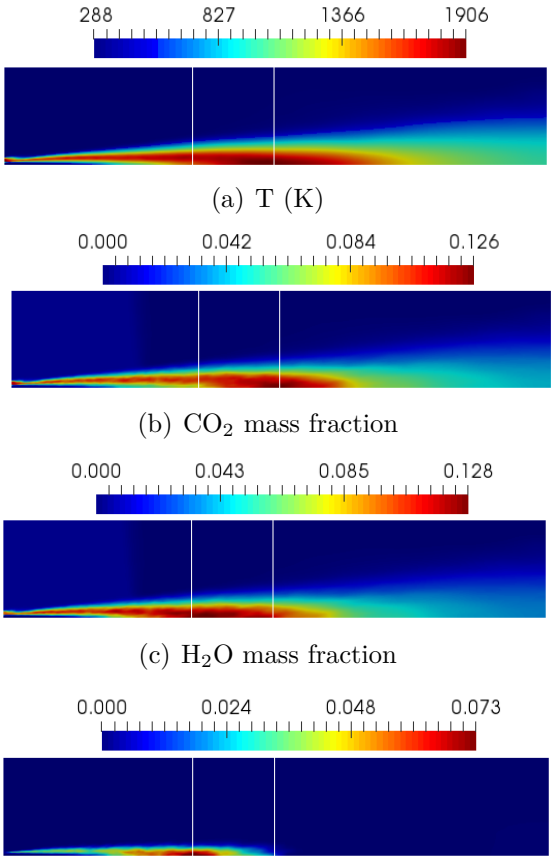

(a) T (K)

(b) CO_2 mass fraction

(c) H_2O mass fraction

(d) CO mass fraction

Figure 5.3: Scalar field contours for SandiaDx4 configuration

The results of both methods show excellent agreement with the benchmark case. Results from QMC is always within one standard deviation of MC result. The standard deviation of MC and actual deviation of QMC from the benchmark solution is higher near the centerline. It is because the volume of computational cells near centerline is much smaller and radiation being a volumetric phenomena, the number of rays passing through a cell is also proportional to its volume. Small-volume cells near centerline, therefore, lead to slightly degraded statistics in MC/QMC.

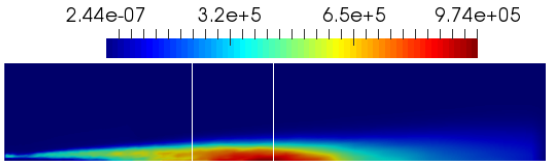

(a) Q_{abs} from benchmark

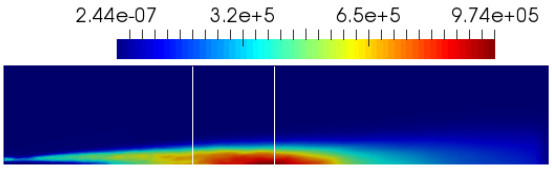

(b) Q_{abs} from MC

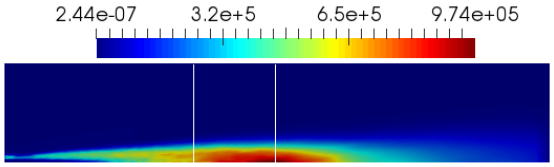

(c) Q_{abs} from QMC

Figure 5.4: Absorption field contours for SandiaDx4 configuration

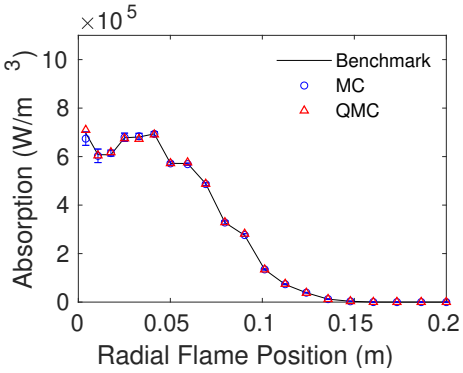

(a) Radial profile along 1.0 m

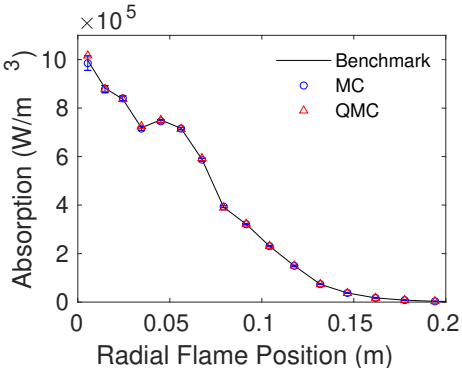

(b) Radial profile along 1.43 m

Figure 5.5: Absorption along a line in SandiaDx4 configuration with 800,000 rays

5.2.2 A High-Pressure Gas Turbine

The second three-dimensional configuration is based on the SGT-100 industrial gas turbine combustor with an output of approximately 5 MW and pressure ratio of approximately 15:1 [56]. Snapshots of the scalar fields are taken from a numerical simulation done by Ren et al [8]. The simulations were performed in a Reynolds averaged Navier Stokes (RANS) framework with standard k-ϵ turbulent model and GRI-Mech 2.11 chemical mechanism [8]. The computational domain is shown in Fig. 5.6, and the scalar fields of the snapshot used in this study are shown in Fig. 5.7. The gas turbine, referred to as the `GT` configuration, has 15,718 finite volume cells for the axisymmetric domain. The walls are considered black and emitting at a temperature 673 K. As before, CO_2, CO, and H_2O are treated as participating media.

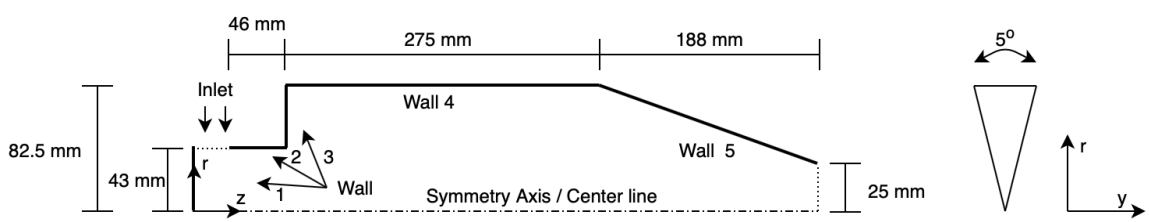

Figure 5.6: GT configuration

The benchmark solution for this case was calculated from 50 statistical MC simulations with 10^7 rays. For performance comparison, both MC and QMC was run with 1.6×10^6 rays. We performed $S = 10$ statistical simulations of MC to obtain statistical mean and standard deviation. The actual scalar field for radiative source term and absorption are almost indistinguishable between benchmark, MC, and QMC runs and hence are not shown here. Instead, we show one axial (at $r = 0.03$ m) and one radial (at $z = 0.1$ m) profile of the absorption as marked in

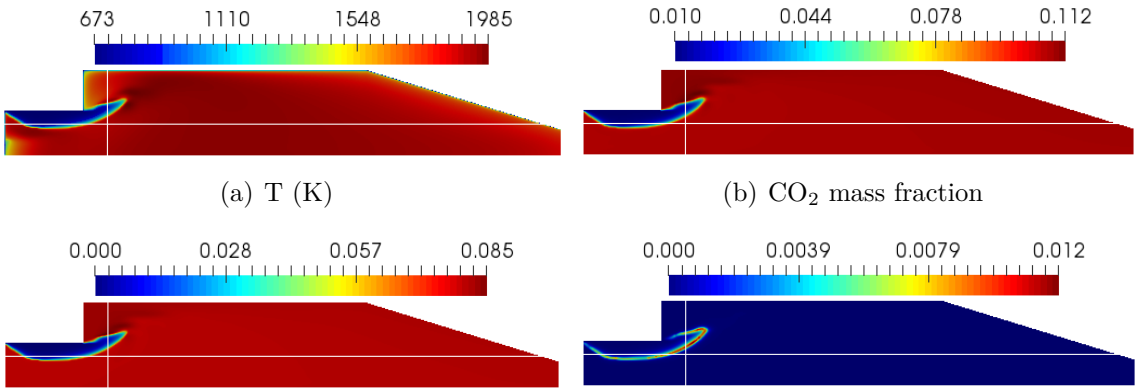

(a) T (K)

(b) CO_2 mass fraction

(c) H_2O mass fraction

(d) CO mass fraction

Figure 5.7: Scalar field contours for GT configuration

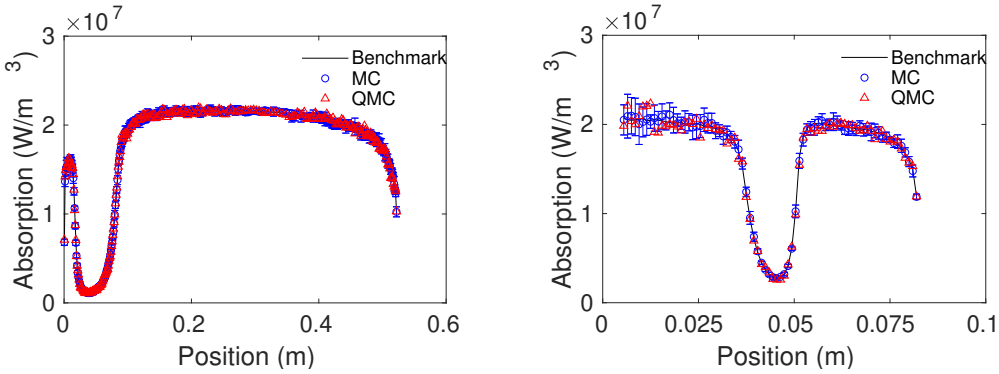

(a) Axial profile along $r = 0.03$ m

(b) Radial profile along $z = 0.1$ m

Figure 5.8: Absorption along a line in GT configuration with 1,600,000 rays

Fig. 5.7. Figure 5.8 shows the local radiative absorption along these lines. Both the MC and QMC methods are in very good agreement with the benchmark solution and the results from QMC fall within one standard deviation of the MC method throughout the lines. As seen before, the standard deviation and error margin increases due to smaller cell volumes near the centerline.

The GT configuration has five walls around the combustion domain. Radiative heat loss to walls is an important quantity. Figure 5.9 shows the wall heat flux of the benchmark, MC, and QMC simulations along walls 4 and 5 shown in Fig. 5.6. It is interesting to see that although the absorption in the media is

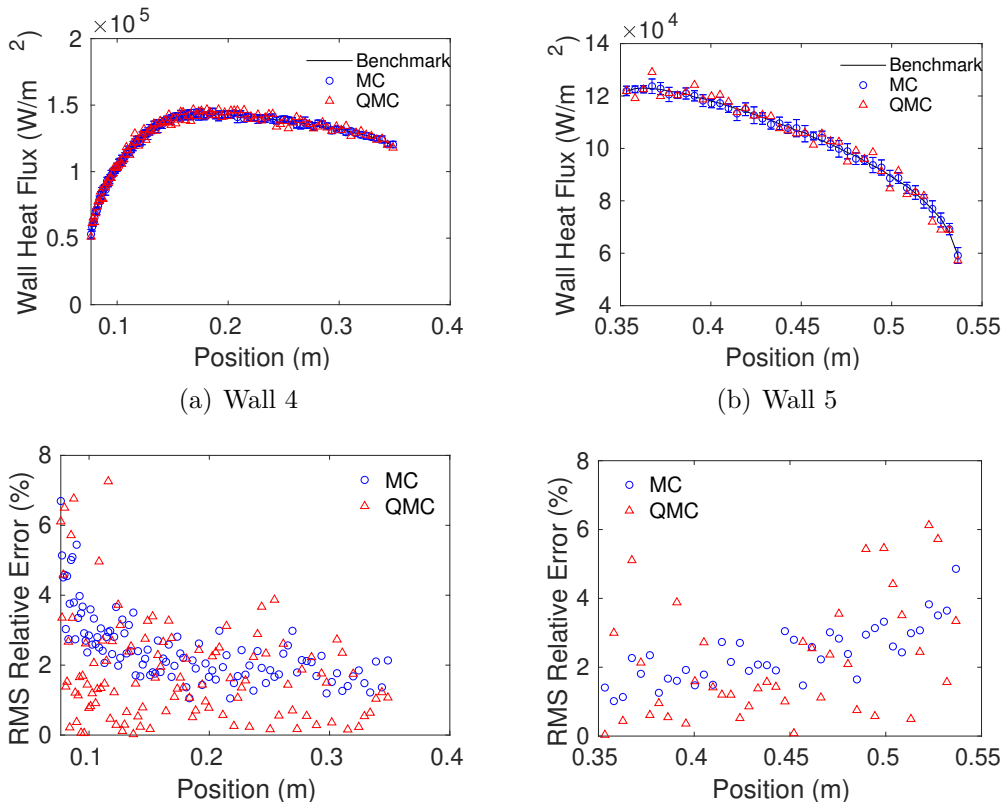

(a) Wall 4

(b) Wall 5

(c) Wall 4 RMS relative error

(d) Wall 5 RMS relative error

Figure 5.9: Wall heat flux in GT configuration with 1,600,000 rays

predicted well by QMC, the wall heat flux results show larger error. In some positions, the result from QMC are outside one standard deviation of the corresponding MC result. However, Fig. 5.9(c) and 5.9(d), which present relative errors for both MC and QMC, indicate that in most locations QMC has lower error than MC. The average relative error in wall heat flux from QMC is less than MC, albeit with a more scattered pattern (*i.e.*, a larger range) in error distribution in QMC. In fact, this trend is seen throughout this study. Figure 5.1(b) also show a similar scatter with a few points in QMC having a slightly larger error than MC.

In this QMC implementation it is expected that including walls will show minor effect on the outcome of the simulation. Because wall faces are planar faces we need two, instead of three, parameters to characterize origin of wall rays (say,

$\mathcal{R}_j^x, \mathcal{R}_j^y$ for MC and $\mathcal{S}_j^1, \mathcal{S}_j^2$ for QMC). Since only five numbers from a six-dimensional sequence are utilized in some rays, there is an expected global loss of "uniformity" within the sequence. However, the effect of this "loss of uniformity" is likely negligible, for two reasons. First, in this GT simulation more than 1.5×10^6 rays were emitted from the participating medium (*i.e.*, internal cells) while approximately 2.5×10^4 rays were emitted from walls. Second, typically any subset of an LDS will also tend to be an LDS. Therefore, overall loss of uniformity is expected to be small because of this dimensional discrepancy between wall-emitted and medium-emitted rays. The dimensionality of low-discrepancy sequences in thermal radiation is discussed further in the next chapter.

5.2.3 ECN Spray-A

The last case considered is from the Engine Combustion Network's (ECN) Spray-A configuration [57]. This configuration, referred to as Spray-A, is a constant volume combustion chamber where liquid n-dodecane is injected as high-pressure spray. The snapshot is taken from the RANS simulations presented in [58, 59] at a time when all spray has evaporated. The configuration is presented in Fig. 5.10. This is also an axisymmetric mesh with 12,800 finite volume computational cells. The walls are hot at 850 K and emits as black surfaces. The peak soot volume fraction in the domain is 7.7 ppm. Along with the LBL data for the participating gases (CO_2, CO, and H_2O) soot is also treated as participating media. Radiative properties of soot are modeled based on the wavelength-dependent correlation [60]. Nature of radiative properties of soot is much closer to black body than the gases, hence we chose a case where there is a significant amount soot. The scalar fields of this case are shown in Fig. 5.11.

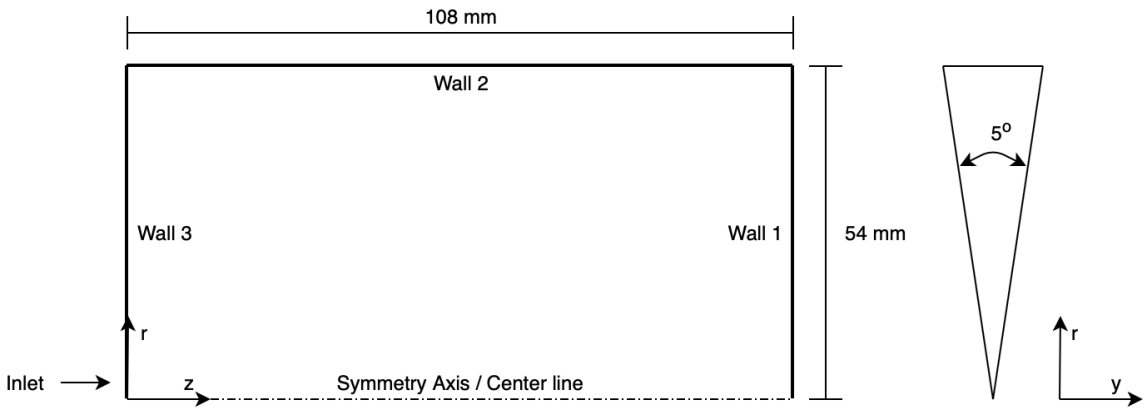

Figure 5.10: Spray A configuration geometry

The benchmark solution for this case was based on the 50 statistical runs of conventional MC with 10^7 rays. The MC and QMC runs for performance comparison purpose was done using 1.6×10^6 rays. As before, $S = 10$ statistical runs were used for MC and only one deterministic run for QMC. As with other cases, we do not show the contour plots of radiative absorption or radiative source term of the benchmark, MC, and QMC simulations, but rather focus on radial and axial profiles. Radiative absorption is compared in Fig. 5.12 along the axial $r = 0.004$ m, and radial $z = 0.105$ m lines marked in Fig. 5.11. Both QMC and MC show agreement with the benchmark solution and the QMC method is within one standard deviation throughout the lines. As before, larger error can be observed near the centerline.

Figure 5.13 shows the wall heat flux results from MC and QMC. While the results at the Wall 1 matches well with the benchmark solution, the Wall 2 results vary wildly. In fact, along Wall 2 not only the standard deviation from the MC is quite large, but also at several locations the QMC results lie beyond one standard deviation from the MC. A point of note here is that the actual value of wall heat flux at Wall 2 is considerably smaller than Wall 1. This indicates the total amount of emission and irradiation on the wall are close. In situations where local emission

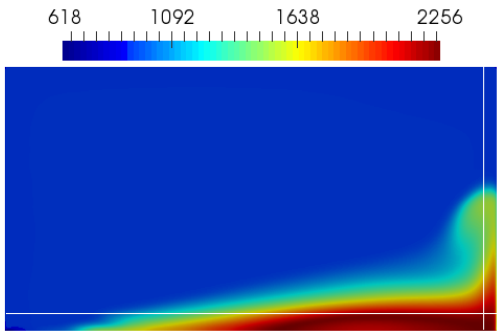

(a) T (K)

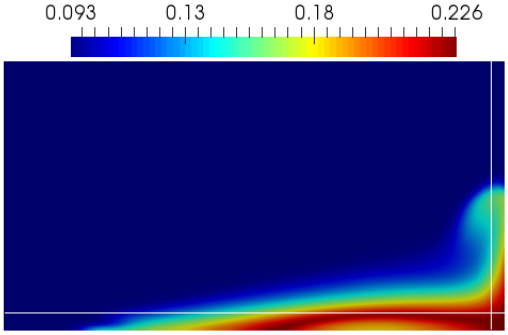

(b) CO_2 mass fraction

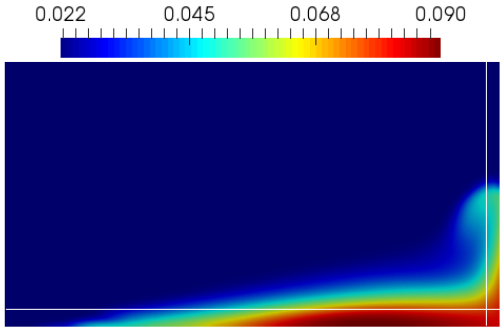

(c) H_2O mass fraction

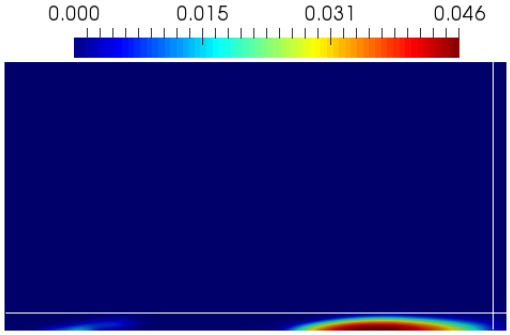

(d) CO mass fraction

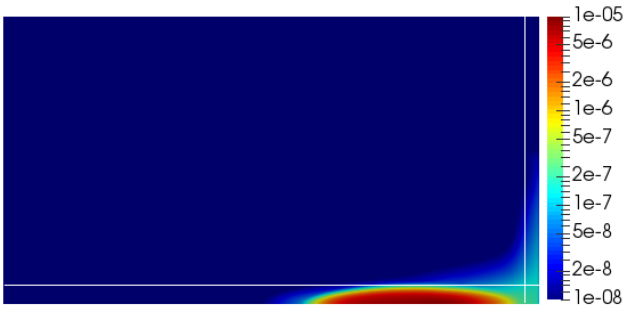

(e) Soot volume fraction

Figure 5.11: Scalar field contours for Spray-A configuration

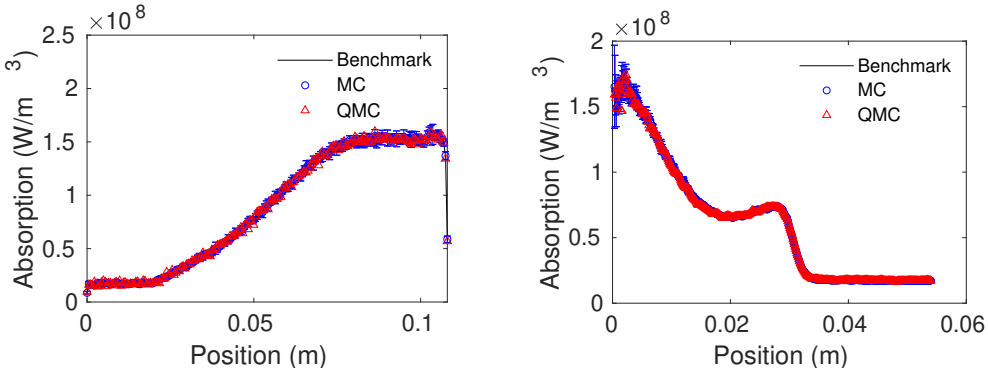

(a) Axial profile along $x = 0.004$ m (b) Radial profile along $z = 0.105$ m

Figure 5.12: Absorption along a line in Spray-A configuration with 1,600,000 rays

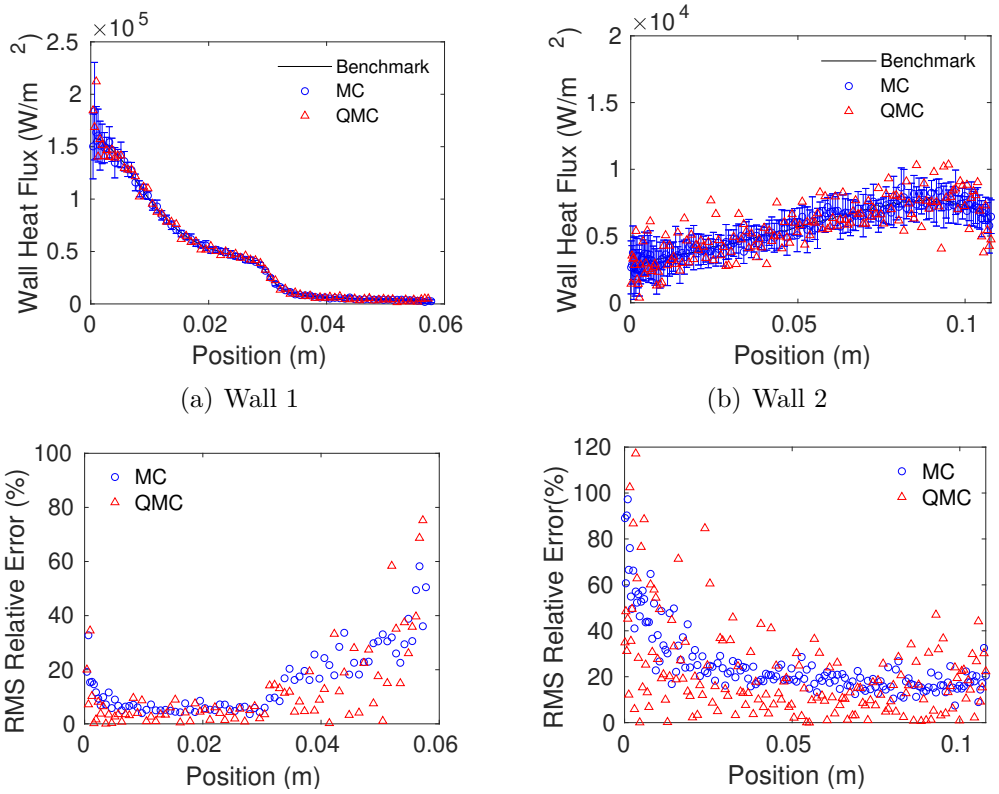

(a) Wall 1 (b) Wall 2

(c) Wall 1 RMS relative error (d) Wall 2 RMS relative error

Figure 5.13: Wall heat flux in Spray-A configuration with 1,600,000 rays illustrated in Fig. 5.10

and irradiation is close to one another (similar to optically thick regions) Monte Carlo methods tend to require more rays to resolve the net radiative transfer. The comparison of relative error in Fig. 5.13(c) and 5.13(d) indicate that both QMC and MC predict the solution well in regions of higher wall flux (Fig. 5.13(c) $r = 0$ to 0.03 m). Another factor contributing to higher relative error in lower heat flux regions is the fact that for computational efficiency, the number of rays generated in a region of a computational domain in current Monte Carlo scheme is proportional to the energy content of the region. Since the region near Wall 2 is comparatively cooler than other regions (Fig. 5.7), the total number of rays in the region near Wall 2 is less than other parts (e.g., near the flame). This leads to higher statistical error near Wall 2.

5.2.4 Computational Efficiency and Figure of Merit

Typically in a Monte Carlo solvers for thermal radiation most of the computational effort is spent in tracing the ray as it requires an exhaustive face-line intersection search at every computational cell each ray goes through. Whereas generation of random numbers and estimation of origin, direction, and wavenumber of a ray is needed to be done only once in a ray's lifetime in absence of any scattering or reflection event. Regeneration of random numbers for a ray is required only when a reflecting wall or a scattering event is encountered. The base Monte Carlo code used in this study spends roughly 90% time in tracing the rays compared to only 10% in generation of random numbers and calculation of origin, direction, and wavenumber of the rays. The computational overhead of Sobol sequence is very similar to that of PRNG algorithm used in the MC simulations in this study. Therefore there were no significant difference in computational effort of a single MC and QMC run with same number of rays.

However, the advantage of QMC can be found when the computational cost is considered along with the statistical accuracy of the simulation. The FoM metric as shown in Eqn. 5.2 gives an idea of this cost-accuracy benefit of QMC. Figure 5.14 shows the FoM based on average RMS relative error along the two lines for each combustion simulation (Sandia Dx4, GT, and Spray A). Since there were 10 statistical simulations of MC as opposed to one deterministic simulation of QMC, the computational runtime is expected to be approximately 10 times more for the MC. This would indicate a factor of $S = 10$ increase in FoM for QMC over MC. Figure 5.14 shows that in all three cases the increase in FoM due to QMC is more than a factor of $S = 10$ and somewhere closer to a factor of 30 to 50. This indicates that QMC not only provides a way to eliminate several statistical runs required for MC, but it can produce a lower statistical error than a single MC simulation. Similar results can be seen in Fig. 5.15, where the FoM is calculated based on the wall heat flux for both the GT and Spray-A configurations. As seen in the wall heat flux comparisons (Figs. 5.9 and 5.13, the error margin for QMC is larger in terms of wall heat flux. This is reflected in reduction of relative advantage in the FoM plots in Fig. 5.15. Nevertheless, even with higher variation in error for the wall heat flux, the FoM of QMC is at least an order of magnitude higher than that of MC.

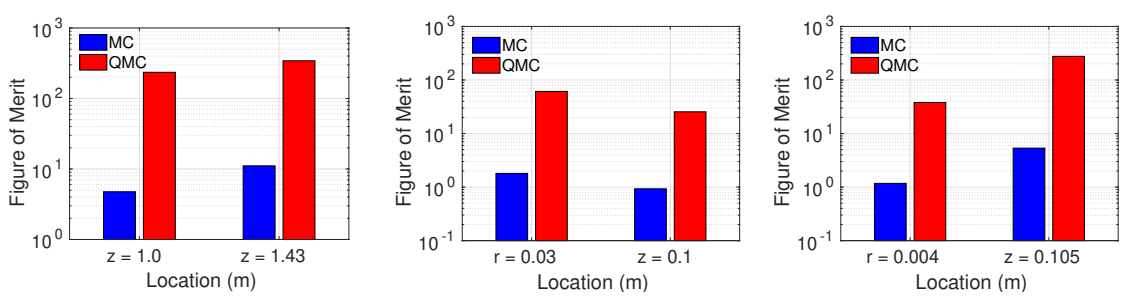

(a) SandiaDx4 with 800,000 rays (b) GT with 1,600,000 rays (c) Spray-A with 1,600,000 rays

Figure 5.14: Figure of Merit (FoM) along two different lines of MC and QMC simulations for SandiaDx4, GT and Spray-A configurations

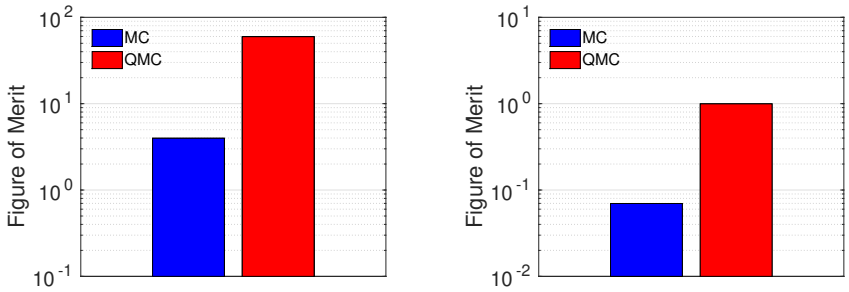

(a) GT with 1,600,000 rays (b) Spray-A with 1,600,000 rays

Figure 5.15: Figure of Merit (FoM) for both walls in the GT and Spray-A configurations in MC and QMC simulations.

5.3 Summary

In this work a Monte Carlo-based radiation solver implemented with a low discrepancy sequence was validated against a one-dimensional slab with a known solution. Afterwards, it was extended into three-dimensional combustion simulations and compared to a benchmark solution to provide a proof-of-concept. In all cases QMC performed better in terms of average RMS relative error while only using one statistical analyses. This coupled effect was shown in the Figure of Merit scores assigned to MC and QMC. This study shows that a QMC method is well suited for thermal radiation and can be considered over traditional MC schemes.

CHAPTER 6

RECOMMENDATIONS FOR QMC

6.1 Choice of Low-Discrepancy Sequence

Selecting Sobol's sequence was somewhat arbitrary as there are many viable low-discrepancy sequences to choose from. Quasi-random sequences have also been developed by Hammersley, Halton, Niedereitter, Faure, and others. In this section, we will compare Halton, Niedereitter and Sobol sequences implemented in the QMC method with the same configurations presented in Chapter 5. The sequences will be validated in one-dimensional plane parallel media and, for brevity, extended to only the gas turbine configuration. We hope to establish a clear-cut, best-fit sequence for thermal radiation in participating media. Because each sequence is generated to have low-discrepancy (*i.e.*, fill n-space with n-tuples as fast as possible), similar accuracy results are expected; however, it is possible that one sequence could have an advantage in terms of computational speed.

A Halton quasi-random sequence is conceptually simple to understand. In one dimension a number, j, is rewritten in base b and the digits are reversed and a preceding decimal point is added. The result is a fraction in base b. Every time j increases, then, the sequence becomes fills the interval from 0 to 1 in a spread out way, because the most significant digit in the fraction, or the last digit in j, changes most rapidly [43]. Halton's sequence in one-dimension is the Van der Corput sequence. Halton generalized this to s-dimensions by using a different prime base for each s.

Niederreiter's quasi-random sequence is a (t, s) sequence in base b. Sobol's sequence can be thought of as a generalized Niederreiter sequence in base 2. Calculation of Niederreiter's sequence occurs in the same manner as Sobol's

sequence with the exception of how direction numbers are generated. Niederreiter's sequence has the smallest discrepancy of all low-discrepancy sequences [61]. For an implemntation comparison of these sequences please see [48, 62]. Figures 6.1, 6.2, and 6.3 illustrate the difference of the three low-discrepancy sequences implemented in this work.

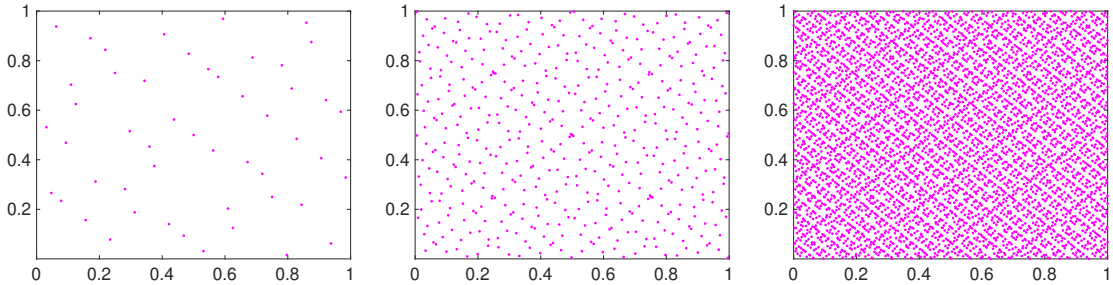

(a) 50 Samples (b) 500 Samples (c) 5000 Samples

Figure 6.1: Two-dimensional Niederreiter Sequence

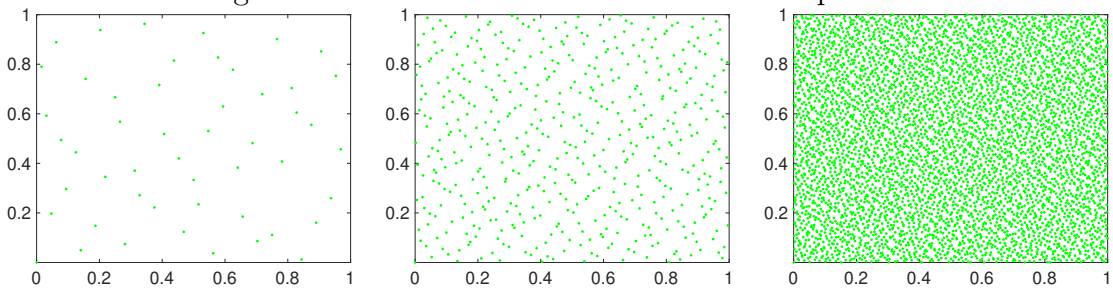

(a) 50 Samples (b) 500 Samples (c) 5000 Samples

Figure 6.2: Two-dimensional Halton Sequence

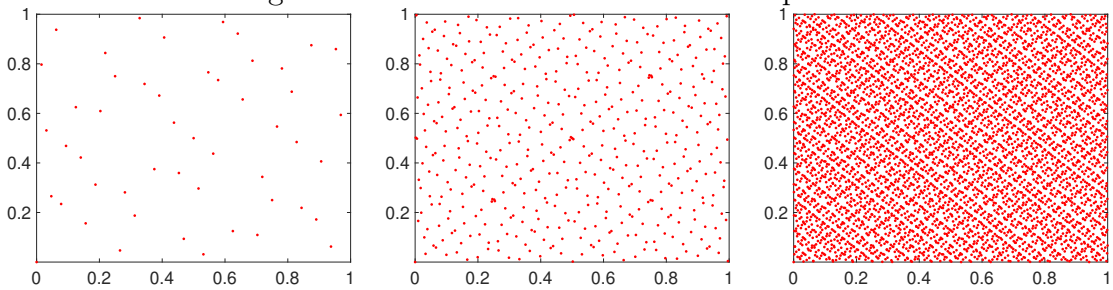

(a) 50 Samples (b) 500 Samples (c) 5000 Samples

Figure 6.3: Two-dimensional Sobol's Sequence

6.1.1 Validation in One-Dimensional Plane-Parallel Media

The configurations presented in this section are the same as presented in Chapter 5. Sobol's, Halton's, Niedereitter's and the standard PMC are all compared simultaneously. Figure 6.4 shows the predicted value of $\nabla \cdot Q$, the RMS relative

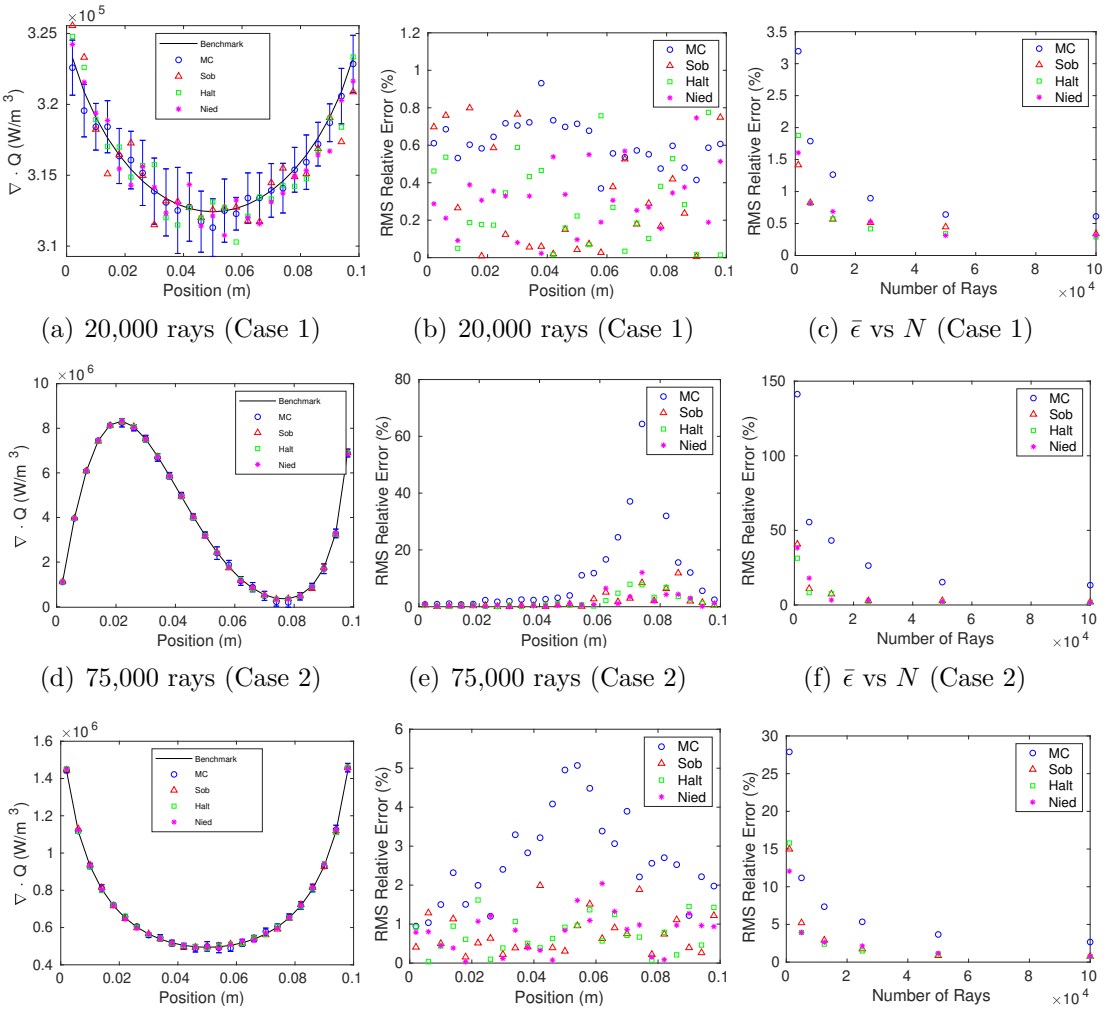

(a) 20,000 rays (Case 1) (b) 20,000 rays (Case 1) (c) $\bar{\epsilon}$ vs N (Case 1)

(d) 75,000 rays (Case 2) (e) 75,000 rays (Case 2) (f) $\bar{\epsilon}$ vs N (Case 2)

(g) 100,000 rays (Case 3) (h) 100,000 rays (Case 3) (i) $\bar{\epsilon}$ vs N (Case 3)

Figure 6.4: Accuracy and convergence of Sobol, Halton, Niedereitter and MC in one-dimensional cases

error, and the convergence of error for each sequence of QMC and MC. Each LDS accurately represents the divergence of heat flux. Furthermore, each LDS has lower

local error and average error compared to the MC method. No distinct advantage for a given LDS is seen in terms of accuracy. Note that computation time of one-dimensional radiative heat transfer is not long enough to calculate a meaningful FoM.

6.1.2 High-Pressure Gas Turbine

We can do a similar study with the gas turbine (GT) combustor as presented in Chapter 5. As a reminder, the GT configuration has a 5 MW output and pressure ratio of approximately 15:1. The snapshot of the scalar fields used in Chapter 5 is used here as well. This configuration has 15,718 finite volume cells in the axisymmetric domain. Walls are black and emit at a temperature of 673 K. The same participating species (CO_2, CO, and H_2O) are used for spectral calculations. Absorption along two lines within the medium, $r = 0.03$ m and $z = 0.1$ m, are shown in Fig. 6.5(a) and 6.5(b), respectively. Similarly, wall heat fluxes for walls 4 and 5 of the GT (see Chapter 5) are shown in Fig. 6.6. These figures show that the LDS are in agreement with the benchmark solutions. For any sample size, Fig. 6.5(c) and 6.5(d) show that the averaged RMS relative error ($\bar{\epsilon}$) for LDS is lower than MC; although, in comparison to each other, no LDS presents a distinct advantage in terms of accuracy. The Figure of Merit (FoM) based on $\bar{\epsilon}$ is used again to analyze the coupled nature of computational cost and accuracy for each simulation. In Fig. 6.7 it is evident that no particular advantage can be given to any of the LDS used in this study. Although unsurprising, it serves as confirmation that there are many equivalent options to implement when considering an LDS-based Monte Carlo method for thermal radiation.

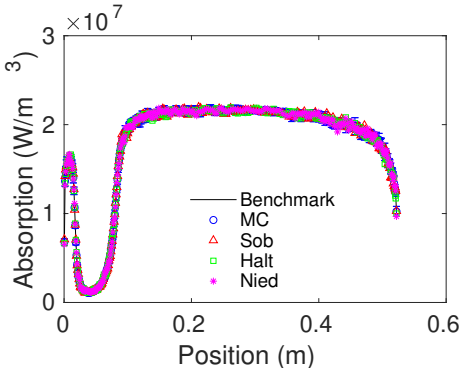

(a) Axial profile along $r = 0.03$ m

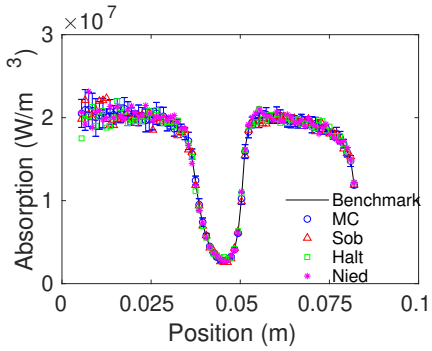

(b) Radial profile along $z = 0.1$ m

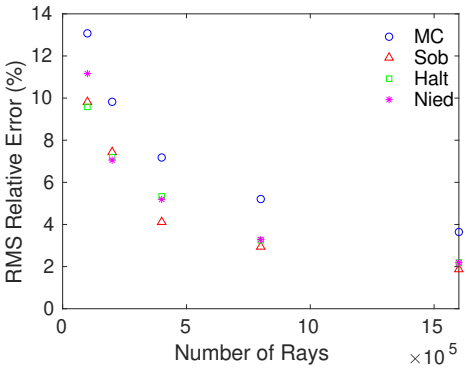

(c) Convergence along $r = 0.03$ m

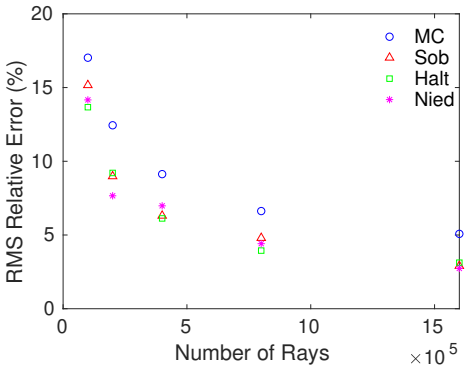

(d) Convergence along $z = 0.1$ m

Figure 6.5: GT medium radiative absorption statistics with 1,600,000 rays

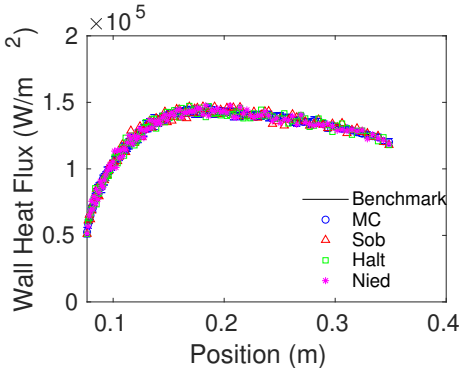

(a) Wall 4

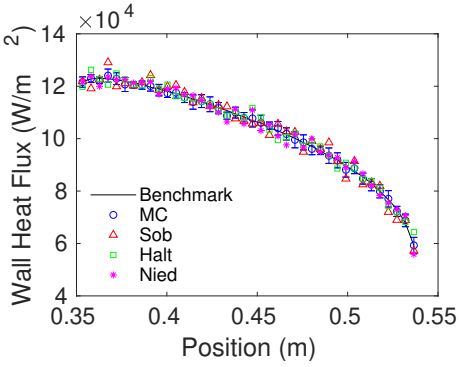

(b) Wall 5

Figure 6.6: Wall heat flux in GT configuration with 1,600,000 rays

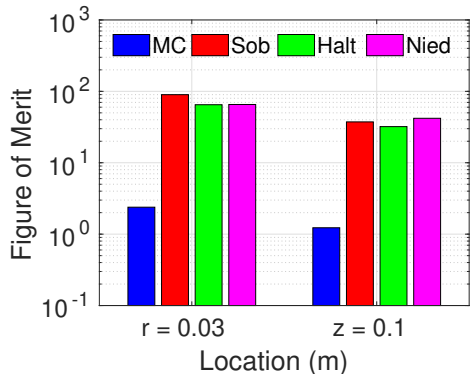

(a) Medium FoM

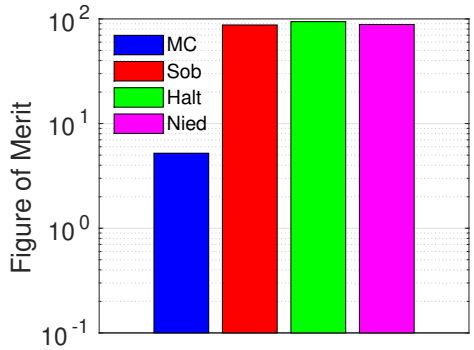

(b) Wall FoM

Figure 6.7: GT FoMs with 1,600,000 rays

6.2 Dimensionality of Low-Discrepancy Sequences

From here on, only Sobol's sequence will be implemented in the quasi-Monte Carlo method because, for one, no distinct advantage is noticeable for any particular low-discrepancy sequence, and two, familiarity. So far it has been implemented as a six-dimensional sequence *i.e.*, $\mathcal{S}^1, \mathcal{S}^2, \ldots, \mathcal{S}^6$ are six, independent sequences. In this section, the dimensionality of the sequence will be further probed.

Sobol's sequence, in this implementation of QMC for thermal radiation, has been inseparable. In one call to the sequence, say emitting a ray from a wall surface, we need two points for emission location $(\mathcal{S}_j^1, \mathcal{S}_j^2)$, two for propagation direction $(\mathcal{S}_j^4, \mathcal{S}_j^5)$ and one for wavenumber $(\mathcal{S}_j^6)$ *i.e.*, in this example, $\mathcal{S}_j^3$ is generated, but not utilized as a wall face is planar. Consequently, there is an

expected global loss of "uniformity" within the sequence. To resolve this, there are a number of ways one could imagine decoupling this sequence *e.g.*, make one call to Sobol for each independent dimension, or couple the sequence in parts by location, direction and wavenumber. The latter is chosen in the new scheme. Therefore, the new scheme will make three calls to Sobol to emit a ray; one for emission location $(\mathcal{S}_j^1, \mathcal{S}_j^2, \mathcal{S}_j^3)$ one for propagation direction $(\mathcal{S}_j^4, \mathcal{S}_j^5)$ and one for wavenumbers $(\mathcal{S}_j^6)$. Of course, emission location will still lose uniformity with wall emission, but now the propagation direction and wavenumbers are independent of this event.

It is likely, however, that the noticeable effect will be marginal at best, for two reasons. First, in the GT configuration, roughly 98% of the rays were emitted from the participating medium. Second, low-discrepancy sequences are distributed in some *self-avoiding* fashion, therefore, any subset within the sequence should also tend to have low-discrepancy.

The new scheme is validated in one-dimensional plane-parallel media and extended to the combustion simulations presented in Chapter 5. For brevity, only a summary of results is provided. See Table 6.1 for results. It can be seen that no

Table 6.1: QMC scheme comparison

Case	$\bar{\epsilon}$ (%)		
	New Scheme	Old Scheme	MC
(1)	0.29	0.31	0.64
(2)	2.59	2.00	15.40
(3)	0.76	0.76	2.51
SandiaDx4	1.05	1.31	2.31
GT	2.78	2.87	5.07
Spray-A	1.51	1.45	3.06

distinct advantage can be attributed to the old scheme and new scheme. The differences in averaged RMS relative error are minute. This aligns with what was

expected because wall emission only account for a tiny fraction of the amount of rays sampled.

6.3 Effect of Reflective Walls

Diffuse reflection, on the other hand, requires the generation of two new random numbers any time a reflection event occurs. This can be a significant addition to the quantity of random numbers drawn in the simulation. Correspondingly, a large number of reflections could considerably effect the "uniformity" of a low-discrepancy sequence and degrade the statistics of the simulation. We will observe the effect of this phenomena in the GT configuration with the new and old scheme, and alternatively, a hybrid scheme that more robustly represents reflection.

6.3.1 High-Pressure Gas Turbine

Each wall in the GT configuration has been modified to be reflective. This was done by lowering the emissivity of each wall by 50%. Again, results from a benchmark solution are used to compare the MC and QMC method. The MC and QMC methods both emitted approximately 1,600,000 rays. This yielded approximately 1,200,000 reflected rays, although this number varied slightly with each method.

Comparison of Old and New Scheme

Figure 6.8 shows the radiaitvie absorption statistics along two lines for both the new and old schemes. Qualitatively, it is observed that each QMC scheme has its own shortcomings. The new scheme in Fig. 6.8(a) shows a good estimation until the trailing edge where the statistics degrade. Figure 6.8(b), shows high scatter

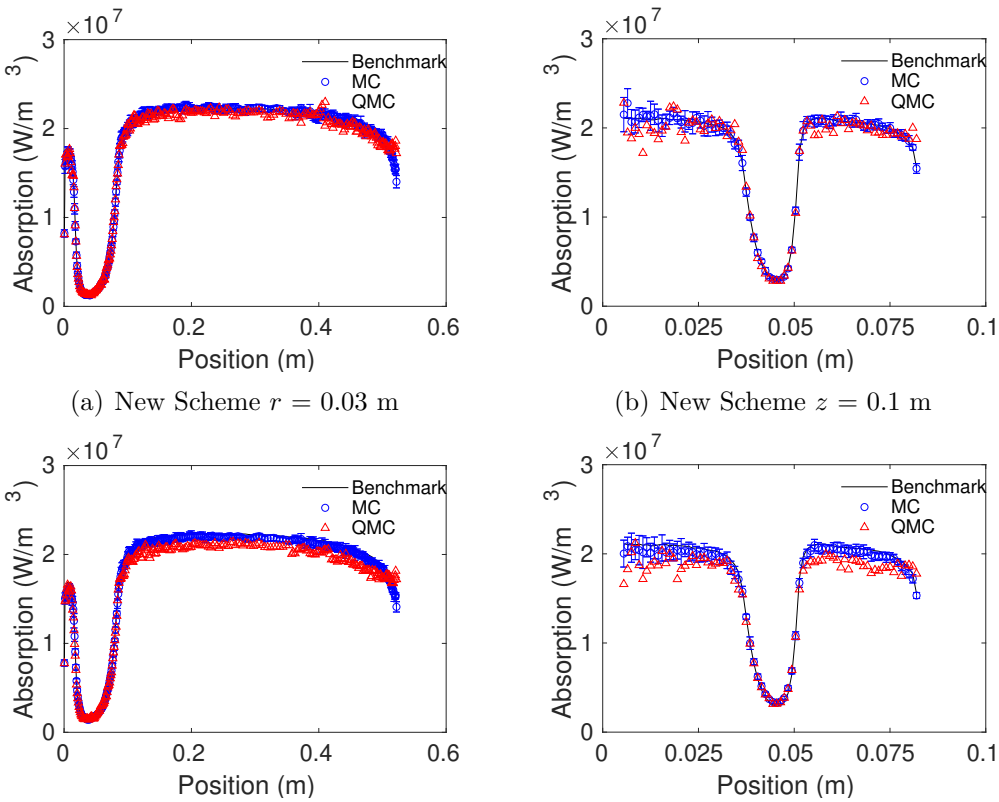

(a) New Scheme $r = 0.03$ m

(b) New Scheme $z = 0.1$ m

(c) Old Scheme $r = 0.03$ m

(d) Old Scheme $z = 0.1$ m

Figure 6.8: GT medium radiative absorption statistics with 1,600,000 rays

throughout the domain, and a similar effect at the trailing edge. The old scheme, Fig. 6.8(c) and 6.8(d), show underestimation of the absorption profile and the same effect at the trailing edge. The degraded performance with reflection can be seen quantitatively in Fig. 6.9(a) and 6.9(b) for the new and old scheme, respectively. While the new scheme shows slight overall improvement when reflection is considered, the FoM is now less than a magnitude of order difference. This indicates that the accuracy of the method is less than that of the MC method.

Hybrid Scheme

Alternatively, a hybrid scheme for QMC was developed to account for reflection more robustly. The hybrid scheme uses the old scheme for QMC with an

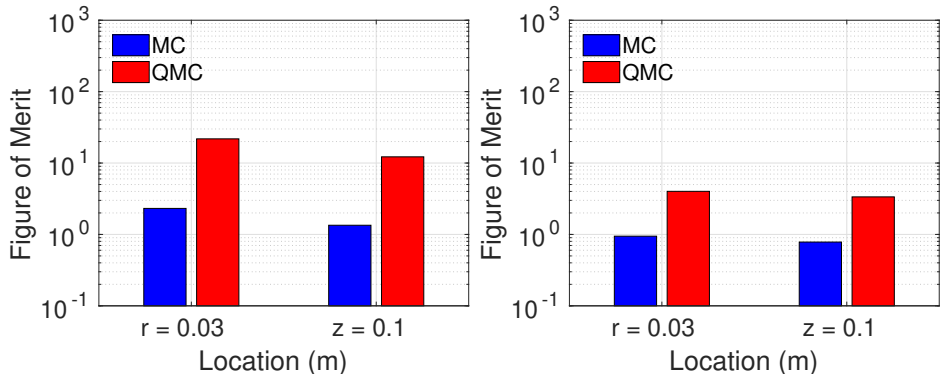

(a) New Scheme FoM (b) Old Scheme FoM

Figure 6.9: GT FoMs with 1,600,000 rays

additional two-dimensional sequence to account for diffuse reflection *i.e.*, $\mathcal{S}_j^1, \mathcal{S}_j^2, \ldots, \mathcal{S}_j^6$ plus an independent $\mathcal{S}_j^7, \mathcal{S}_j^8$ for reflection events. This ensures that the rays will be reflected uniformly with low-discrepancy without a loss in discrepancy. The benefit of the hybrid scheme is shown in Fig. 6.10. Qualitatively it is shown that the absorption profile is more accurately predicted than the previous methods. Furthermore, in Fig. 6.10(c), it is shown that the FoM is at least an order of magnitude higher than MC, which indicates that the hybrid scheme has an advantage in both accuracy and computational cost.

6.4 Summary

This chapter presented a discussion of how best to implement a QMC method for thermal radiation which was facilitated through results from example cases. First, the choice of low-discrepancy sequence for use in a QMC method was shown to have negligible impact. Then, the effect of wall emission was addressed by introducing a new scheme to eliminate loss of discreapncy, but it was shown that, again, the effect was negligible because the large percentage of rays are emitted from a participating medium. Finally, the effect of reflection was considered. Diffuse reflection requires the generation of two new random numbers and this was shown

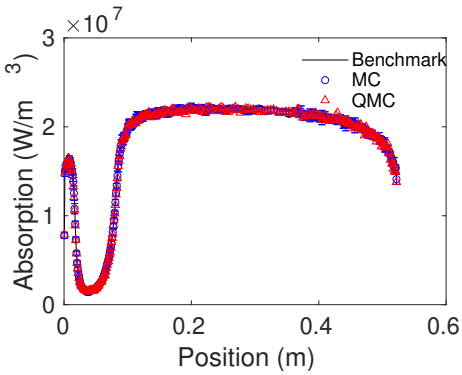

(a) Hybrid Scheme $r = 0.03$ m

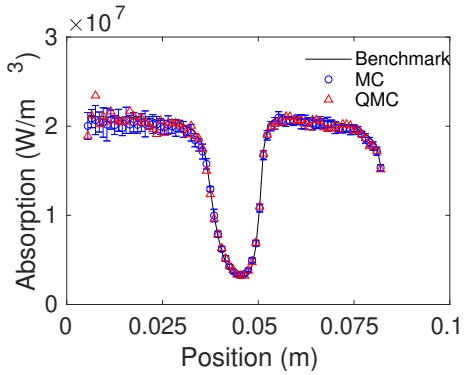

(b) Hybrid Scheme $z = 0.1$ m

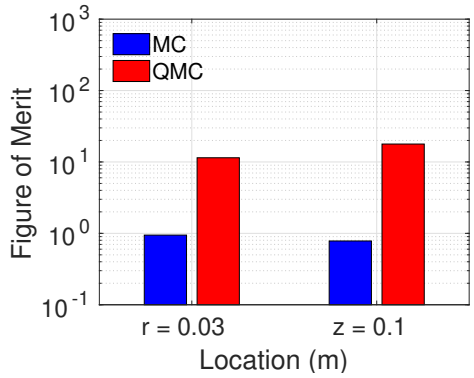

(c) Hybrid Scheme FoM

Figure 6.10: GT FoMs with 1,600,000 rays

to have an adverse effect on the two QMC schemes. A hybrid method was developed to address reflection events that considerably improved the results.

CHAPTER 7

CONCLUSION

Radiative heat transfer in participating media is among the most challenging computational engineering problems due to the complex nature of the radiation transport. The relevance of thermal radiation in high temperature applications (*e.g.*, combustion) has prompted the development of many approximate models (*e.g.*, the discrete ordinate method, method of spherical harmonics, optically thin approximation, etc.). Despite shortcomings of these approximations, many of them are implemented in commercial computational fluid dynamics (CFD) solvers to reduce computational complexity and costs. Monte Carlo ray tracing (MCRT) schemes are the most accurate solvers for thermal radiation and can be easily extended to any complex configuration while retaining accuracy. The main bottleneck for Monte Carlo (MC) methods is the computational cost due to the significant number of rays that must be sampled. This work addressed the bottleneck by replacing the random number sampling mechanism in traditional MC methods with a low-discrepancy sequence (LDS). A systematic performance analysis was done on the accuracy and computational cost of the developed QMC method. Additionally, recommendations were given for QMC implementation strategy in terms of the different low discrepancy sequences – Sobol, Halton, and Niederreiter – used, and the dimensionality of the sequence.

The QMC method was validated in several one-dimensional configurations. It was shown that QMC has comparable accuracy to traditional Monte Carlo methods in optically thin and optically thick gray media, while similar results were obtained for nongray media. Then, QMC was extended to three-dimensional snapshots of combustion simulations. It was shown that, in terms of local and averaged RMS relative error, that QMC has comparable accuracy in these

simulations as well. It was advantageous to compare MC with QMC via a Figure of Merit (FoM). This metric illustrated the coupled effect of computational expense and accuracy where a higher FoM is indicative of a good MC scheme. For any given simulation, the FoM was higher for QMC than MC. The main source of this was the computational cost. Traditional MC methods are probabilistic and therefore require repeated sampling. In this work, the performance comparisons were run with ten statistical analyses (*i.e.*, ten repeated, independent simulations). The QMC method, on the other hand, is deterministic and required just one simulation. This effectively reduced the computational cost by an order of magnitude. In principle, then, the computational cost of QMC will scale at least by $1/s$ where S is the number of simulations run. In practice the gain in FoM was found to be more than S-fold. In conclusion, QMC is a viable alternative to traditional Monte Carlo methods for radiative heat transfer calculations in high-fidelity simulations because of the significant decrease in computational cost with comparable accuracy.

CHAPTER 8

FUTURE WORK

Outlook on future research for the quasi-Monte Carlo (QMC) method can be lumped into three broad categories. First, continue to explore the quasi-Monte Carlo method in relevant combustion simulations. The current work studied snapshot cases of combustion simulations. The QMC method should be extended to full coupled simulations of combustion, and similarly, compared with a benchmark Monte Carlo method. Second, although the computational cost of QMC scales fractionally with $1/s$ to the MC method (where S is the number of simulations), it would be worthwhile to perform a formal comparative analysis in terms of computational cost and accuracy to other deterministic solvers (*e.g.*, discrete ordinate method, method of spherical harmonics, etc.). It would be useful in this stage to also analyze how well the QMC scales in parallel computing runs. Collectively, this would provide a clear answer to whether the QMC method *should* be adopted or not for commercial solvers in practice. Third, the algorithm of the QMC method should continue to be addressed. This study documented the choice of different low-discrepancy sequences and the best way to implement a sequence in terms of its dimensionality as it relates to thermal radiation. Since results varied for three different implementations a more exhaustive study on the effect of dimensionality should be done. Some guidelines were given, such as using an independent sequence for reflection events, but an optimal structure has yet to be determined. Moreover, there are additional phenomena that have yet to be accounted for such as scattering due to particulate media. The algorithmic QMC method can be fundamentally modified, as well, which is another area of potential exploration. Randomized quasi-Monte Carlo (RQMC) methods are sometimes implemented in order to run a simulation S times to get S independent results [63].

These are also referred to as variance reduction techniques for Monte Carlo methods, and have varying degrees of success. A full study on these three fronts will provide a more robust and clear outlook on the future of QMC in practice.

BIBLIOGRAPHY

[1] M. F. Modest. *Radiative Heat Transfer*. Academic Press, 2013.

[2] Michael Modest and Daniel Haworth. *Radiative Heat Transfer in Turbulent Combustion Systems*. Springer, 2015.

[3] Sandip Mazumder and Michael F. Modest. A pdf approach to modeling turbulence-radiation interactions in nonluminous flames. 2006.

[4] Mohammad Naraghi, Sade Dunn, and Douglas Coats. Modeling of radiation heat transfer in liquid rocket engines. 07 2005.

[5] Florian Goebel, Björn Kniesner, Manuel Frey, Oliver Knab, and Christian Mundt. Radiative heat transfer analysis in modern rocket combustion chambers. *CEAS Space Journal*, 6:79–98, 06 2014.

[6] G Pal, A Gupta, M F Modest, and D C Haworth. Comparison of accuracy and computational expense of radiation models in simulation of nonpremixed turbulent jet flames. *Combustion and Flame*, 162:2487–2495, 2015.

[7] Somesh Roy, Jian Cai, Wejun Ge, and Michael Modest. Computational cost and accuracy comparison of radiation solvers with emphasis on combustion simulations. volume 18 of *6*, pages 1493–1510. International Symposium on Advances in Computational Heat Transfer, 2015.

[8] T. Ren, M. F. Modest, and S. Roy. Monte Carlo Simulation for Radiative Transfer in a High-Pressure Industrial Gas Turbine Combustion Chamber. *Journal of Engineering Gas Turbines and Power*, 140(5):051503, 2017.

[9] A. Wang, M. F. Modest, D. C. Haworth, , and L. Wang. Monte Carlo simulation of radiative heat transfer and turbulence interactions in methane/air jet flames. *Journal of Quantitative and Spectroscopic Radiative Transfer*, 109:269–279, 2008.

[10] Joseph A. Farmer and Somesh P. Roy. A quasi-monte carlo method for thermal radiation in participating media. *Journal of Quantitative and Spectroscopic Radiative Transfer*, Submitted, 2019.

[11] H. C. Hottel and E. S. Cohen. Radiant heat exchange in a gas-filled enclosure: Allowance for nonuniformity of gas temperature. *AIChE Journal*, 4(1):3–14.

[12] Arthur H. Lefebvre. Flame radiation in gas turbine combustion chambers. *International Journal of Heat and Mass Transfer*, 27(9):1493 – 1510, 1984.

[13] R. Viskanta and M.P. Mengüç. Radiation heat transfer in combustion systems. *Progress in Energy and Combustion Science*, 13(2):97 – 160, 1987.

[14] S. Chandrasekhar. *Radiative Heat Transfer*. Dover Publications, 1960.

[15] J.H. Jeans. The equations of radiative transfer of energy. *Royal Astronomy Society*, 78:28–36, 1917.

[16] Wenjun Ge, T. Ren, Michael F. Modest, S Roy, and Daniel C. Haworth. Application of high-order spherical harmonics methods for radiative transfer in simulation of a turbulent jet flame. In *Proceedings of CHT-17, ICHMT International Symposium on Advances in Computational Heat Transfer*, Napoli, Italy, 2017.

[17] Wenjun Ge, Michael F. Modest, and Ricardo Marquez. Two-dimensional axisymmetric formulation of high order spherical harmonics methods for radiative heat transfer. *Journal of Quantitative Spectroscopy and Radiative Transfer*, 156:58–66, 2015.

[18] Wenjun Ge, Michael F. Modest, and Somesh P. Roy. Development of high-order PN models for radiative heat transfer in special geometries and boundary conditions. *Journal of Quantitative Spectroscopy and Radiative Transfer*, 172:98—-109, 2015.

[19] Michael F. Modest and Jun Yang. Elliptic PDE formulation and boundary conditions of the spherical harmonics method of arbitrary order for general three-dimensional geometries. *Journal of Quantitative Spectroscopy and Radiative Transfer*, 109(9):1641–1666, 2008.

[20] Wenjun Ge, Ricardo Marquez, Michael F. Modest, and Somesh P. Roy. Implementation of high-order spherical harmonics methods for radiative heat transfer on OpenFOAM. *Journal of Heat Transfer*, 137(5):052701, 2015.

[21] B Davison. *Neutron transport theory*. Oxford : Clarendon Press, 1957. Bibliography: p. [439]-441.

[22] L. S. Rothman, I. E. Gordon, R. J. Barber, H. Dothe, R. R. Gamache, A. Goldman, V. I. Perevalov, S. A. Tashkun, and J. Tennyson. HITEMP, the high-temperature molecular spectroscopic database. *Journal of Quantitative Spectroscopy & Radiative Transfer*, 111(15):2139–2150, 2010.

[23] Tao Ren and Michael Modest. Line-by-line random-number database for monte carlo simulations of radiation in combustion system. *Journal of Heat Transfer*, 141, 10 2018.

[24] Michael F. Modest. Narrow-band and full-spectrum k-distributions for radiative heat transfer—correlated-k vs. scaling approximation. *Journal of Quantitative Spectroscopy and Radiative Transfer*, 76(1):69 – 83, 2003.

[25] Hongmei Zhang and Michael Modest. A multi-scale full-spectrum correlated-k distribution for radiative heat transfer in inhomogeneous gas mixtures. *Journal of Quantitative Spectroscopy and Radiative Transfer*, 73:349–360, 04 2002.

[26] Anquan Wang and Michael F. Modest. High-accuracy, compact database of narrow-band k-distributions for water vapor and carbon dioxide. *Journal of Quantitative Spectroscopy and Radiative Transfer*, 93(1):245 – 261, 2005. Fourth International Symposium on Radiative Transfer.

[27] Jian Cai and Michael F. Modest. Improved full-spectrum k-distribution implementation for inhomogeneous media using a narrow-band database. *Journal of Quantitative Spectroscopy and Radiative Transfer*, 141:65 – 72, 2014.

[28] Chaojun Wang, Wenjun Ge, Michael F. Modest, and Boshu He. A full-spectrum k-distribution look-up table for radiative transfer in nonhomogeneous gaseous media. *Journal of Quantitative Spectroscopy and Radiative Transfer*, 168:46 – 56, 2016.

[29] W. Reiher. Hammersley, j. m., d. c. handscomb: Monte carlo methods. methuen & co., london, and john wiley & sons, new york, 1964. vii + 178 s., preis: 25 s. *Biometrische Zeitschrift*, 8(3):209–209, 1966.

[30] Pedro Andreo. Monte carlo simulations in radiotherapy dosimetry. *Radiation Oncology*, 13:121, 2018.

[31] Hassan Ali, Nameeqa Firdous, Shumaila Naz, Fakhra Ghafoor, and Sana Saghir. Use of monte carlo methods in biomedical applications. 11 2015.

[32] Jukka Koivisto. Monte carlo path tracing. 03 2019.

[33] Jing Zhao, Yaoqi Duan, and Xiaojuan Liu. Uncertainty analysis of weather forecast data for cooling load forecasting based on the monte carlo method. *Energies*, 11:1900, 07 2018.

[34] Ole Stenzel, L. Jan Anton Koster, Ralf Thiedmann, Stefan D Oosterhout, J. RenéA., Maarten C. W. Janssen, and Volker Schmidt. A new approach to

model-based simulation of disordered polymer blend solar cells. 2011.

[35] Robert H. Swendsen and Jian-Sheng Wang. Nonuniversal critical dynamics in monte carlo simulations. *Phys. Rev. Lett.*, 58:86–88, Jan 1987.

[36] A. Wang and M. F. Modest. Spectral Monte Carlo models for nongray radiation analyses in inhomogeneous participating media. *Int. J. Heat Mass Transfer*, 50:3877–3889, 2007.

[37] T. Ren and M. F. Modest. Hybrid wavenumber selection scheme for line-by-line photon Monte Carlo simulations in high-temperature gases. *ASME Journal of Heat Transfer*, 135(8):084501, 2013.

[38] Michael Modest and S C. Poon. Determination of three-dimensional radiative exchange factors for the space shuttle by monte carlo. *American Society of Mechanical Engineers (Paper)*, 09 1977.

[39] F. James. A review of pseudoranom number generators. *Computer Physics Communications*, 60:329–344, 1990.

[40] S. K. Park and K. W. Miller. Random number generators: Good ones are hard to find. *Communications of the ACM*, 31(10):1192–1201, 1988.

[41] I. Kant, P. Guyer, and A.W. Wood. *Critique of Pure Reason*. Oeuvre. Cambridge University Press, 1999.

[42] Donald E. Knuth. *The Art of Computer Programming, Volume 2 (3rd Ed.): Seminumerical Algorithms*. Addison-Wesley Longman Publishing Co., Inc., Boston, MA, USA, 1997.

[43] William H. Press. *Numerical Recipes*. University of Cambridge, 1986.

[44] H. Niederreiter. Quasi-monte carlo methods and pseudo-random numbers. *American Mathematical Society*, 84:957–1041, 1978.

[45] Harald Niederreiter. *Random Number Generation and quasi-Monte Carlo Methods*. Society for Industrial and Applied Mathematics, Philadelphia, PA, USA, 1992.

[46] I.M Sobol'. On the distribution of points in a cube and the approximate evaluation of integrals. *USSR Computational Mathematics and Mathematical Physics*, 7(4):86 – 112, 1967.

[47] I. A. Antonov and V. M. Saleev. An economic method of computing lpτ - sequences. *USSR Computational Mathematics and Mathematical Physics*, 19:252–256, 1979.

[48] P. Brately and B.L. Fox. Algorith 659: Implementing Sobol's quasirandom sequence generator. *ACM Transactions on Mathematical Software*, 14:88–100, 1988.

[49] Russel E. Caflisch. Monte carlo and quasi-monte carlo methods. *Acta Numerica*, 7:1–49, 1998.

[50] Hans Babovsky, Frank Gropengieer, Helmut Neunzert, Jens Struckmeier, and Bernd Wiesen. Application of well-distributed sequences to the numerical simulation of the boltzmann equation. *Journal of Computational and Applied Mathematics*, 31(1):15 – 22, 1990.

[51] R. Ohbuchi and M. Aono. Quasi-Monte Carlo rendering with adaptive sampling. Technical report, IBM Tokyo Research Laboratory, 1996. http://www.kki.yamanashi.ac.jp/õhbuchi/online_pubs/eg96_html/eg96.htm.

[52] M.B. Giles, F.Y. Kudo, I.H. Sloan, and B.J. Waterhouse. Quasi-monte carlo for finance applications. *Journal of Australian Mathematical Society*, 50:308–323, 2008.

[53] A. Wang and M. F. Modest. Photon Monte Carlo simulation for radiative transfer in gaseous media represented by discrete particle fields. *J. Heat Transfer*, 128:1041–1049, 2006.

[54] R. S. Barlow and J. H. Frank. Effects of turbulence on species mass fractions in methane/air jet flames. *Proceedings of Combustion Institute*, 27:1087 – 1095, 1998.

[55] G. Li and M. F. Modest. Importance of turbulence-radiation interaction in turbulent diffusion flames. *ASME Journal of Heat Transfer*, 125:831 – 838, 2003.

[56] Siemens. SGT-100. http://www.energy.siemens.com/us/en/fossil-power-generation/gas-turbines/sgt-100.htm.

[57] Lyle Pickett, Caroline Genzale, Gilles Bruneaux, Louis-Marie Malbec, Laurent Hermant, and Jesper Shramm. Comparison of diesel spray combustion in different high-temperature, high pressure facilities. *SAE International*, 3:156–181, 2010.

[58] Khaled Mosharraf Mukut and Somesh P Roy. A Sensitivity Study on Soot and NOx Formation in High Pressure Combustion System. In *2018 Spring Technical Meeting of Central States Section of the Combustion Institute*, Minneapolis, MN, USA, 2018.

[59] Khaled Mosharraf Mukut and Somesh Roy. An Investigation of Soot Evolution in High-pressure Spray Combustion. In *11th US National Combustion Meeting*, pages 1–9, Pasadena, CA, 2019.

[60] H Chang and T. T. Charalampopoulos. Determination of the wavelength dependence of refractive indices of flame soot. *Proceedings of the Royal Society A*, 430:577—-591, 1990.

[61] I. L. Dalal, D. Stefan, and J. Harwayne-Gidansky. Low discrepancy sequences for monte carlo simulations on reconfigurable platforms. In *2008 International Conference on Application-Specific Systems, Architectures and Processors*, pages 108–113, July 2008.

[62] Paul Bratley, Bennett L. Fox, and Harald Niederreiter. Implementation and tests of low-discrepancy sequences. *ACM Trans. Model. Comput. Simul.*, 2(3):195–213, July 1992.

[63] Art B. Owen. Quasi-monte carlo sampling. In *SIGGRAPH 2003*, 2003.

APPENDIX A

APPENDIX

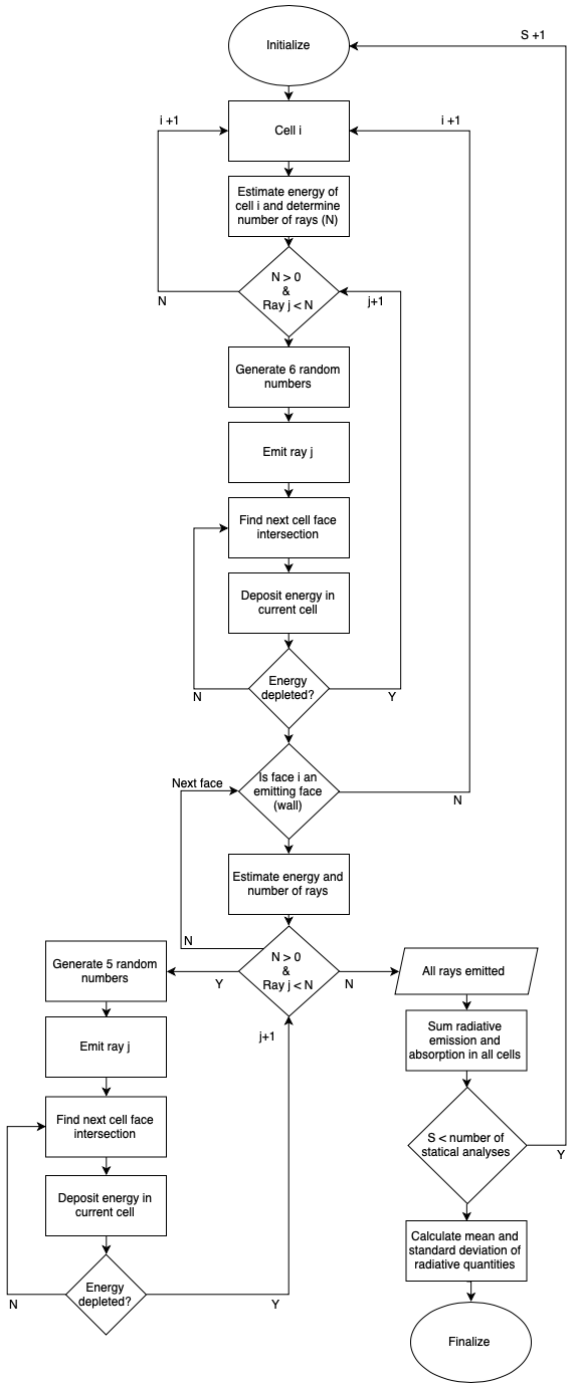

Figure A.1: Flow Chart of photon Monte Carlo method